Published in final edited form as:
Prog Nucl Magn Reson Spectrosc. 2015 February ; 0: 14–32. doi:10.1016/j.pnmrs.2014.11.001.

NMR Studies of Dynamic Biomolecular Conformational Ensembles

Dennis A. Torchia
Building 5, Room 128, NIH, Bethesda, MD 20892-0520 USA, Phone: 301-496-5750, FAX: 301-496-0825, dtorchia@dir.nidcr.nih.gov

Abstract

Multidimensional heteronuclear NMR approaches can provide nearly complete sequential signal assignments of isotopically enriched biomolecules. The availability of assignments together with measurements of spin relaxation rates, residual spin interactions, J-couplings and chemical shifts provides information at atomic resolution about internal dynamics on timescales ranging from ps to ms, both in solution and in the solid state. However, due to the complexity of biomolecules, it is not possible to extract a unique atomic-resolution description of biomolecular motions even from extensive NMR data when many conformations are sampled on multiple timescales. For this reason, powerful computational approaches are increasingly applied to large NMR data sets to elucidate conformational ensembles sampled by biomolecules. In the past decade, considerable attention has been directed at an important class of biomolecules that function by binding to a wide variety of target molecules. Questions of current interest are: “Does the free biomolecule sample a conformational ensemble that encompasses the conformations found when it binds to various targets; and if so, on what time scale is the ensemble sampled?” This article reviews recent efforts to answer these questions, with a focus on comparing ensembles obtained for the same biomolecules by different investigators. A detailed comparison of results obtained is provided for three biomolecules: ubiquitin, calmodulin and the HIV-1 trans-activation response RNA.

Keywords

Hamiltonian; Spin; Relaxation; Residual Dipolar Coupling; Order Parameter; Dynamics

1. Introduction

Theoretical and experimental work directed at using NMR to study molecular dynamics in solution and solid state was initiated shortly after the first successful NMR experiments in bulk matter. By 1960, the basic theory relating magnetic resonance measurements to molecular dynamics had been developed [1]. The introduction of one-dimensional pulsed Fourier transformation spectroscopy [2] opened the way to the first atomic-resolution studies of protein dynamics in solution [3–7]. However, the available methodology limited

---

measurements to a few resolved and assigned signals. Such measurements have been extended to sites throughout biomolecules, in solution and solid state, by the development of robust sequential assignment methods. These methods [8–10] involve the application of multidimensional heteronuclear spectroscopy to biomolecules uniformly or specifically labeled with $^{2}H/^{13}C/^{15}N$. It is now commonplace to measure relaxation rates, J-couplings, chemical shifts, residual anisotropic interactions (dipolar, quadrupolar and chemical shifts), relaxation dispersion profiles, and magnetization- and hydrogen-exchange rates of biomolecules. Analysis of such measurements yields site-specific information about dynamics on timescales in the range of ps to s [11–20].

While many types of measured NMR parameters are highly sensitive to molecular motions, the data do not directly provide information about atomic positions as a function of time. Molecular dynamics (MD) calculations have the potential to provide this information over an increasingly wide range of timescales. Because of imperfections in force fields, the accuracy of such calculations diminishes as the length of the simulation increases. However, the availability of large NMR data sets that are sensitive to molecular structure and dynamics provide restraints that offer the means of selecting conformations from a calculated ensemble that are in accord with experimental measurements. This prospect has stimulated many investigations in which NMR measurements together with MD calculations are used to determine conformational ensembles that elucidate biomolecular function. Of particular interest have been biomolecules that perform numerous functions by binding to a wide variety of target molecules. Two questions of interest are: “Does the free biomolecule sample a conformational ensemble that encompasses the conformations found when it binds to various targets, and if so, on what time scale is the ensemble sampled?”

This field has been the subject of a recent comprehensive review [18]. Our overview is more narrowly focused and describes sustained efforts over the past decade to answer the questions posed in the previous paragraph in the case of three target-binding biomolecules, ubiquitin, calmodulin and the HIV-1 trans-activation response RNA (TAR). Large NMR data sets, consisting principally of residual dipolar couplings and relaxation rates, measured in both solution and solid state, have been accumulated for these biomolecules. Initially, model-free (MF) approaches were used to extract estimates of rates and amplitudes of internal motions of individual atomic sites or of domains. More recently, NMR data have been used in conjunction with all-atom computational approaches to derive ensembles of conformations sampled by these systems on the ps-ms timescale.

In view of the vast number of degrees of freedom needed to define the dynamics of even a small biomolecular ensemble, such an enterprise faces considerable challenges. This review was motivated by an interest in comparing ensembles of the same biomolecules that have been determined independently by different groups of investigators using somewhat different approaches. It is thought that such a comparison should help reveal both the progress made and challenges that remain for such studies.

As most data sets used to derive the ensembles discussed herein consisted of residual spin interactions (e.g. dipolar couplings) and relaxation rates, an overview of the theory used to interpret such measurements is first presented. This is followed by a brief summary of experimental approaches used to make such measurements. Then the studies of the dynamics of ubiquitin, calmodulin and TAR are reviewed and results obtained by different groups are compared. The paper closes with a brief perspective based upon the results obtained for these biomolecules.

2. Theoretical background

2.1. Orientation-dependent spin-interaction Hamiltonians

Most studies of biomolecular dynamics have involved measurements of either residual anisotropic interactions (couplings) and/or relaxation rates of ^{2}H, ^{13}C, or ^{15}N spins. The theory that accounts for such measurements is well established [1, 21–25]. Herein it is presented in a form that is readily applicable to studies of biomolecular dynamics carried out in both solution and solid state.

The dominant orientation-dependent spin interactions for ^{13}C and ^{15}N are dipole-dipole couplings (D) and chemical shifts (CS), while for ^{2}H, the quadrupolar interaction (Q) dominates. Stochastic motions that modulate these interactions lead to spin relaxation of these nuclei. The Hamiltonians, H_λ, of the three interactions, λ = D, CS, Q, can be expressed using either second-rank Cartesian or spherical tensors. An advantage of the latter is that every H_λ can be written as a scalar product of two tensors, T^λ and R^λ, where the interaction tensor R^λ does not contain any spin operators, which are all contained in T^λ. When T^λ and R^λ are expressed in a laboratory (L) frame in which Z_L is parallel to B_0, the external field, H_λ in frequency units (s^{-1}), is given by [23]:

$$H_\lambda = C^\lambda \sum_{m=-2}^{2} (-1)^m T^\lambda_{2m} R^\lambda_{2-m} \quad (1)$$

The constants C^λ and spin operators T^λ are defined in Table 1. The interaction tensor, R^λ, is most simply expressed in its principal axis system (PAS) or P-frame, where it is specified by only two elements ρ^λ_{20} and $\rho^\lambda_{22} = \rho^\lambda_{2-2}$ (Table 1), which are available from experiment. The R^λ_{2m} are obtained from the ρ^λ_{2m} according to [23]

$$R^\lambda_{2-m} = \sum_{n=-2}^{2} \rho^\lambda_{2\mathrm{n}} D^2_{n-m}(\Omega_{PL}) \quad (2)$$

where D^2_{pq} are Wigner rotation matrix elements [26] and rotation of the P-frame through Euler angles $\Omega_{PL} = (\alpha_{PL}\beta_{PL}\gamma_{PL})$ brings it into coincidence with the L-frame. The closure (addition) theorem for the Wigner matrix elements [26] yields

$$R^\lambda_{2-m} = \sum_{q,n=-2}^{2} \rho^\lambda_{2\mathrm{n}} D^2_{nq}(\Omega_{PM}) D^2_{q-m}(\Omega_{ML}) \quad (3)$$

where rotation through Euler angles $\Omega_{PM} = (\alpha_{PM}\beta_{PM}\gamma_{PM})$ brings the P-frame into coincidence with an intermediate frame, e.g., the molecule-fixed M-frame, Fig. 1, and subsequent rotation of the M-frame through Euler angles $\Omega_{ML} = (\alpha_{ML}\beta_{ML}\gamma_{ML})$ brings it into coincidence with the L-frame. The entire orientation dependence of H_λ is described by

Wigner matrix elements that have well-known transformation properties under rotations [26]. An appropriate choice of the M-frame facilitates calculation of spin Hamiltonians that are averaged by rotations. This, in turn, expedites calculations of residual couplings and spin relaxation in the presence of molecular motions in both solids and liquids.

2.2 The heteronuclear dipolar spin Hamiltonian

We now consider the dipolar interaction between an isolated pair of spin-1/2 unlike nuclei *I* and *S*, which we take as *I* = ^{1}H and *S* =^{15}N as this is the most relevant situation for the applications considered in this review. In this case, as seen in Table 1, $\rho^{\lambda}_{2n} = 0$ unless n = 0 (because the dipolar tensor is axially symmetric) and H_D is given by

$$H_D = -\sqrt{6}\omega_D \sum_{m=-2}^{2} (-1)^m T_{2m}^D \sum_{q=-2}^{2} D_{0q}^2(\Omega_{PM}) D_{q-m}^2(\Omega_{ML}) \ where, \ \omega_D = (\mu_o/4\pi)\gamma_I\gamma_S\hbar/r_{IS}^3 \quad (4)$$

The frequencies of the two ^{15}N (S-spin) transitions (corresponding to the proton being in either |α> or |β> states) are orientation-dependent. Because the magnitude of the ^{15}N Zeeman frequency ($\gamma_S B_0$) is much greater than that of the orientation-dependent part of the transition frequency, the latter can be calculated using first-order perturbation theory and the secular, m = 0, component of H_D. $D^2_{q0}(\Omega_{ML})$ and D^2_{0q} (Ω_{PM}) are spherical harmonics [26] and are therefore functions of only two Euler angles, (β_{ML},α_{ML}) and (β_{PM},γ_{PM}), respectively. Further, $(\beta_{ML},\alpha_{ML}) = \Omega_B = (\theta_B,\varphi_B)$ and $(\beta_{PM},\pi\text{-}\gamma_{PM}) = \Omega_\mu = (\theta_\mu,\varphi_\mu)$, where Ω_μ and Ω_B are spherical polar angles of unit vectors $\boldsymbol{\mu}_B$ (parallel to B_0) and $\boldsymbol{\mu}$ (parallel to the ^{15}N-^{1}H bond axis), respectively, Fig. 2. Using these angles and the secular part of $T_{20}{}^D$, Table 1, one obtains the secular Hamiltonian

$$H_D = -2\omega_D \hat{I}_z \hat{S}_z \sum_{q=-2}^{2} C_{2q}^*(\Omega_B) C_{2q}(\Omega_\mu) \ where, \ C_{2q}^*(\Omega_B) = D_{q0}^2(\Omega_{ML}), C_{2q}(\Omega_\mu) = D_{0q}^2(\Omega_{PM}) \quad (5)$$

and C_{2q} are modified spherical harmonics [26]. When the proton spin state is |β>, first-order perturbation theory yields the orientation-dependent part of the ^{15}N transition frequency

$$\omega = \omega_D \sum_{q=-2}^{2} C_{2q}^*(\Omega_B) C_{2q}(\Omega_\mu) \quad (6)$$

The sign of ω reverses when the ^{1}H spin state is |α>. On rotation of coordinates, the $C_{2q}(\Omega_B)$ and $C_{2q}(\Omega_\mu)$ transform as elements of symmetric second-rank spherical tensors, designated T^B and T^μ. Therefore ω is the scalar product of T^B and T^μ tensors whose symmetry axes are along $\boldsymbol{\mu}_B$ and $\boldsymbol{\mu}$. Because ω is a scalar it is unaffected by a rotation of the M-coordinate frame relative to $\boldsymbol{\mu}_B$ and $\boldsymbol{\mu}$, and therefore depends only on θ, the angle between $\boldsymbol{\mu}_B$ and $\boldsymbol{\mu}$, Fig. 2, the principal axes of T^B and T^μ. This result follows from Eq. (6) using the addition theorem of spherical harmonics [26], which yields

$$\omega = \omega(\theta) = \omega_D P_2(\cos\theta) \quad (7)$$

Although Eq. (6) is more complex than Eq. (7), it will be seen that the former equation facilitates calculations of ω and relaxation rates in the presence of molecular reorientation.

As a consequence of the angular dependence of ω, the ^{15}N signal is very broad (~10^4 Hz) in solid powders. The lineshape is a superposition of signals corresponding to the ^{1}H |α> and |β> spin states (a Pake doublet), Fig. 3A. The dipolar coupling, in Hz, for each value of θ is the difference between ω(α) and ω(β) divided by 2π, or $d_C = -\omega(\theta)/\pi$, with maximum value $D_{max} = -\omega_D/\pi$, yielding

$$d_C = D_{\max} P_2(\cos\theta) = D_{\max} \sum_{q=-2}^{2} C^*_{2q}(\Omega_B) C_{2q}(\Omega_\mu) \quad (8)$$

Note that the units of d_c are Hz while those of ω are radians/s. In view of the trivial difference between ω(α) and ω(β), we henceforth consider only the latter, and it is to be understood that ω = ω(β).

2.3 Motional averaging of the ^{15}N-^{1}H dipolar interaction

We discuss the averaging of the orientation-dependent part of the transition frequency using either ω or d_c, in accordance with established usage. When all rates of reorientation are much greater than ω_D, (the so-called fast limit, where the time dependence of ω is negligible to first order) the averages of ω and d_c are obtained by replacing the right sides of Eqs. (6) and (8) by spatial ensemble averages taken over all orientations.

$$\langle\omega\rangle = \omega_D \sum_{q=-2}^{2} \left\langle C^*_{2q}(\Omega_B)\right\rangle \langle C_{2q}(\Omega_\mu)\rangle \quad (9)$$

$$\langle d_c\rangle = D_{\max} \sum_{q=-2}^{2} \left\langle C^*_{2q}(\Omega_B)\right\rangle \langle C_{2q}(\Omega_\mu)\rangle \quad (10)$$

Note that in writing Eqs. (9) and (10) we have assumed that the motions of $\boldsymbol{\mu}_B$ and $\boldsymbol{\mu}$ are uncorrelated so that their ensemble averages can be calculated independently. We now consider how various types of motions in the solid state and in solution average ω and d_c.

2.3.1 Sample spinning in the solid state—

To calculate <ω>, we fix the M-frame relative to the L-frame and take Z_M (the Z axis of the M-frame) along the sample spinning axis. This axis subtends an angle θ with $\boldsymbol{\mu}_B$ (which is along Z_L), and because the L and M-frames are fixed relative to one another, rotation of the sample about Z_M does not affect $C_{2q}(\Omega_B)$. In contrast, for q = ±1, ±2, < $C_{2q}(\Omega_\mu)$> vanishes once per rotor cycle, because $C_{2q}(\Omega_\mu)$ is proportional to $\exp(iq\varphi_\mu)$. The q = 0 term contains the factor $C_{20}(\Omega_B) = P_2(\cos\theta_B)$, which scales every dipolar coupling by a function that vanishes when $\theta_B = \arccos(1/\sqrt{3}) \approx 54.7°$, the magic angle, whence <ω> = 0. This result also applies to the CS interaction, even though the CS tensor is generally asymmetric, because an asymmetric tensor can be written as the sum of two axially symmetric tensors [27]. Therefore, ultra-fast (beyond ca 60 kHz) magic angle spinning (MAS) yields high-resolution ^{15}N spectra of solids whose signals appear at their isotropic (liquid-like) frequencies. More commonly, lower spinning rates can eliminate small CS anisotropies (CSA) and weak dipolar interactions, involving ^{15}N and ^{13}C spins, while high-power ^{1}H decoupling can suppress strong ^{1}H-^{15}N and ^{1}H-^{13}C dipolar couplings.

Because <ω> vanishes only once every rotor cycle, the MAS spectrum consists of sharp signals at the isotropic frequencies, flanked by sidebands at multiples of the spinning frequency [28–30]. When proton decoupling is applied and the spinning rate is much greater than ω_{CS} the sideband intensities are negligible. Conversely, when the spinning rate is low while proton decoupling is applied, the sideband intensities can be used to obtain the principal components of the static (or the dynamically averaged) chemical shift tensors [28–30]. Generally, information contained in anisotropic interactions can be obtained by applying suitable RF pulses in synchronism with MAS, thereby interfering with the averaging produced by spinning, a technique called 'recoupling'. Dipolar recoupling allows one to retain information (e.g., internuclear distances) provided by dipolar interactions and, at the same time, record high-resolution spectra [31–34].

2.3.2 Internal N-H bond motions in a solid—We now consider a non-spinning solid composed of un-oriented, immobile biomolecules that contain N-H bonds that sample an ensemble of conformations. We fix the M-frame in the molecule, and the conformational ensemble sampled by an N-H bond in this frame is defined by an equilibrium probability distribution function [35], $p_{eq}(\Omega_\mu)$, where $p_{eq}(\Omega_\mu)d\Omega_\mu$ is the probability of finding $\boldsymbol{\mu}$ in solid angle $d\Omega_\mu$ centered at Ω_μ. If all reorientation rates are much larger than ω_D, Eq. (9) becomes

$$\langle\omega\rangle=\omega_D\sum_{q=-2}^{2}C^*_{2q}(\Omega_B)\left\langle C_{2q}(\Omega_\mu)\right\rangle \quad (11)$$

where the ensemble averages

$$\langle C_{2q}(\Omega_\mu)\rangle=\int p_{eq}(\Omega_\mu)C_{2q}(\Omega_\mu)d\Omega_\mu \quad (12)$$

are spherical order parameters that contain information about p_{eq}. To show this, we first note that because p_{eq} depends only upon the polar angles $\Omega_\mu=(\theta_\mu,\varphi_\mu)$, it can be expanded in terms of the complete set of spherical harmonics.

$$p_{eq}(\Omega_\mu)=\sum_{l=0}^{\infty}\sum_{m=-1}^{1}a_{1m}C^*_{lm}(\Omega_\mu) \quad (13)$$

Multiplying both sides of this equation by $C_{kq}(\Omega_\mu)$, integrating over Ω_μ, and using the orthogonality property of the spherical harmonics yields, $a_{kq} = [(2k+1)/4\pi]<C_{kq}>$. With this result

$$p_{eq}(\Omega_\mu)=\sum_{k=0}^{\infty}[(2k+1)/4\pi]\sum_{q=-k}^{k}\langle C_{kq}\rangle\,C^*_{kq}(\Omega_\mu) \quad (14)$$

For brevity, we write $<C_{2q}>$ as S_q and note that while the infinite set of S_q determine p_{eq}, at most, only five of the order parameters needed to do so, S_q $(-2 \le q \le 2)$, can be obtained from measurements of <ω>.

The S_q are elements of the spherical tensor $\langle T^{\mu}\rangle$. When the PAS frame of $\langle T^{\mu}\rangle$ and the M-frame are coincident, $S_{\pm 1} = 0$ and $S_2 = S_{-2}$ [23] and Eq. (11) becomes

$$\langle\omega\rangle = (\omega_D/2)S_0\left[3\cos^2\theta_B - 1 + \sqrt{6}(S_2/S_0)\sin^2\theta_B\cos 2\phi_B\right] \quad (15)$$

This equation is usually written in terms of principal frequencies $\langle\omega_X\rangle$,$\langle\omega_Y\rangle$,$\langle\omega_Z\rangle$, the values taken by $\langle\omega\rangle$ when $\boldsymbol{\mu}_B$ is along the principal axes of $\langle T^{\mu}\rangle$, X_{μ},Y_{μ},Z_{μ}, respectively. When $\boldsymbol{\mu}_B$ is along Z_{μ}, $\theta_B = 0$ and $\langle\omega_Z\rangle/\omega_D = S_0$. In similar fashion, $\langle\omega_X\rangle/\omega_D = -S_0/2+\sqrt{6}S_2/2$, and $\langle\omega_Y\rangle/\omega_D = -S_0/2-\sqrt{6}S_2/2$, where the convention $|\langle\omega_Z\rangle| \geq |\langle\omega_X\rangle| \geq |\langle\omega_Y\rangle|$ is used and $|z|$ means absolute value of z. Eq. (15) then becomes

$$\langle\omega\rangle = (\langle\omega_Z\rangle/2)\left[3\cos^2\theta_B - 1 - \eta\sin^2\theta_B\cos 2\phi_B\right] \quad (16)$$

where (θ_B,φ_B) are the polar angles of $\boldsymbol{\mu}_B$ in the PAS of $\langle T^{\mu}\rangle$, the asymmetry parameter, $\eta = (\langle\omega_Y\rangle - \langle\omega_X\rangle)/\langle\omega_Z\rangle$, equals zero when $\langle T^{\mu}\rangle$ is axially symmetric. The powder lineshape, $I(\omega)$, corresponding to the angular dependence of $\langle\omega\rangle$ is an elliptic integral [22, 23], an example of which is plotted in Fig. 3B. This lineshape, rather than the Pake doublet, Fig. 3A, is observed when the N-H bond axis executes a two-site 60° jump as described in the figure legend. In this example $\eta = 0.6$ and $\langle\omega_Z\rangle = (5/8)\omega_D$.

The five individual S_q provide useful information about p_{eq} when the orientation of the PAS frame of $\langle T^{\mu}\rangle$ is known in the M-frame. This information is not available in a sample consisting of randomly oriented molecules. However, the averaged principal frequencies obtained from the lineshape yield the following two rotationally invariant combinations [36, 37] of the S_q

$$\sum_{q=-2}^{2}|S_q|^2 = 2(\omega_1^2+\omega_2^2+\omega_3^2)/3 = \omega_3^2(1+\eta^2/3) = S^2 \quad (17)$$

and

$$\sum_{npq=-2}^{2} S_n S_p S_q \begin{pmatrix} 2 & 2 & 2 \\ n & p & q \end{pmatrix}\begin{pmatrix} 2 & 2 & 2 \\ 0 & 0 & 0 \end{pmatrix}^{-1} = 4(\omega_1^3+\omega_2^3+\omega_3^3)/3 = 4\omega_1\omega_2\omega_3 = \omega_3^3(1-\eta^2) \quad (18)$$

where S^2 is the MF generalized order parameter [38], the large parentheses denote Wigner 3-j symbols [26], and $\omega_1 = \langle\omega_X\rangle/\omega_D$, $\omega_2 = \langle\omega_Y\rangle/\omega_D$, $\omega_3 = \langle\omega_Z\rangle/\omega_D$. A distribution function $p_{eq}(\Omega_{\mu})$ that correctly describes the conformational ensemble sampled by $\boldsymbol{\mu}$ must yield order parameters that satisfy these equations, whatever orientation is chosen for the M-frame in the biomolecule.

2.3.3 Alignment of rigid biomolecules in solution—We next consider a biomolecule that diffuses as a rigid body in solution, and fix the M-frame in the molecule. In an isotropic liquid, the $C_{2q}(\Omega_{\mu})$ are not averaged by overall diffusion because $\boldsymbol{\mu}$ is fixed in the M-frame; in contrast, all $\langle C_{2q}(\Omega_B)\rangle$ vanish because $p_{eq}(\Omega_B) = 1/4\pi$. Therefore, according to Eq. (10), $\langle d_c\rangle$, the residual dipolar coupling (RDC) also vanishes. However, as first shown by Saupe

[39], RDCs can be observed when molecules are weakly aligned by a liquid-crystalline medium. Uniaxial alignment of biomolecules has been achieved using liquid crystals, strained gels and external fields [40–42]. Note that from the perspective of the M-frame, $\boldsymbol{\mu}_B$ has non-uniform distribution of orientations, $p^A{}_{eq}(\Omega_B)$, as a consequence of molecular alignment. The five accessible alignment order parameters, $\langle C_{2q}(\Omega_B)\rangle$, are elements of $\langle T_B\rangle$, where the ensemble average is over the orientations of $\boldsymbol{\mu}_B$ in the M-frame and $\langle T^B\rangle$ is called the alignment tensor. Accordingly, we abbreviate the $\langle C_{2q}(\Omega_B)\rangle$ as $S_q{}^A$, to distinguish them from the S_q introduced in Eq. (15). For each N-H site, j = 1, 2, …, N, the RDC_j is a linear function of the $S_q{}^A$

$$RDC_j = D_{\max}\sum_{q=-2}^{2} S_q^A C_{2q}(\Omega_{\mu j}) \quad (19)$$

When N ≥ 5, these equations can be used to obtain the $S_q{}^A$ using singular value decomposition [37, 43], (SVD) if the coordinates $\Omega_{\mu j}$ are known (in some M-frame), as is the case when the structure of the biomolecule is known. The elements of the 3×3 Saupe order matrix are readily obtained from the $S_q{}^A$ [37, 40, 42], and diagonalization of the order matrix yields the orientation of the $\langle T^B\rangle$ PAS [37, 43]. In this frame, $S_{\pm1}{}^A = 0$, $S_2{}^A = S_{-2}{}^A$ and proceeding as with Eq. (16) one finds

$$RDC_j = (D_{\max}/2)A\left[3\cos^2\theta_{\mu j} - 1 - \eta_A \sin^2\theta_{\mu j}\cos 2\phi_{\mu j}\right] \quad (20)$$

where, $A = S_0{}^A$, $\eta_A = -\sqrt{6}S_2{}^A / S_0{}^A$ are called the magnitude and asymmetry of the alignment tensor, and $(\theta_{\mu j},\varphi_{\mu j})$ are the polar angles of $\boldsymbol{\mu}_j$ in the PAS of the alignment tensor. In the PAS frame of the alignment tensor, $S_0{}^A = S_{ZZ}{}^A$ and $\sqrt{6}S_2{}^A = (S_{YY}{}^A - S_{XX}{}^A)$, where $S_{ii}{}^A$ are elements of the Saupe order tensor.

Eq. (20) has the same form as Eq. (16) because in the case of alignment, $\boldsymbol{\mu}_B$ plays the role that $\boldsymbol{\mu}$ had in the case of NH bond dynamics in a solid. For this reason, a histogram of dipolar couplings has the functional form of a solid-state powder pattern, I(ω), e.g. as shown in Fig. 3B when the NH bond orientations are uniformly distributed in the aligned biomolecule. Also, equations for alignment order parameters, $S_q{}^A$, have been derived [37] that are analogs of Eqs. (17) and (18). This reference [37] also contains the generalization of Eq. (19) that applies in the case of an asymmetric interaction tensor (e.g. an arbitrary chemical shift tensor).

A biomolecule having a large anisotropic magnetic susceptibility, χ, will spontaneously align in a strong external magnetic field. However, diamagnetic alignment of biomolecules is typically so weak that RDCs cannot be measured accurately. Considerably stronger magnetic alignment has been achieved by attaching to biomolecules paramagnetic tags (such as lanthanides or spin-labels) that have large anisotropic χ-tensors. Pseudocontact shifts (PCSs) are also observed in such samples. In the PAS system of the χ-tensor, the angular dependence of RDC_j and PCS_j is given by Eq. (20). The complete expressions for these quantities, in terms of the magnitude and anisotropy of the χ-tensor, are given by Bertini et al.[44].

As a consequence of their sensitive dependence on the orientation of the NH bonds relative to a molecular frame, RDCs have been widely used as restraints in determining the three-dimensional structures of biomolecules. They provide global orientational restraints that have significantly improved the quality of structures of proteins and nucleic acids determined by NMR [40, 41, 45]. RDCs have also been used to cross-validate crystal structures and NMR structures obtained without using RDC restraints.

2.3.4 Alignment of biomolecules containing two domains—In addition to providing structural information about biomolecules, RDCs have also been used to obtain information about the structures and relative motions of biomolecules containing two domains. It is most straightforward to do this when one domain is entirely responsible for alignment. This has been achieved using lanthanides in the case of calmodulin [46], and domain extension in the case of TAR RNA [47]. In the latter case, the domain responsible for alignment is axially symmetric. The five order parameters, S_q^A, characterizing relative motions of the domains are obtained from the alignment tensors determined for each of the two domains [48]. In the general case, where the alignment tensor of the domain responsible for alignment is asymmetric, the order parameters are ensemble averages of Wigner rotation matrix elements [49]. If five independent alignments are available, twenty-five such order parameters can be obtained, thus representing the maximum amount of model-independent information that can be obtained from RDC measurements about the distribution function describing the relative motions of the two domains [49].

It is generally not possible to determine the probability distribution function sampled by a biomolecule composed of two domains from the limited number of order parameters obtained from RDC data. Therefore RDCs, together with other NMR data, have recently been used in combination with computational all-atom approaches to determine dynamic ensembles of such systems [18, 50–53]. Later in this paper we compare ensembles independently determined using this approach by different groups for the same biomolecule.

2.3.5 Alignment of biomolecules containing mobile N-H bonds—RDCs of amides are impacted by motions of N-H bonds in the molecular frame [42], which we take as the M-frame. Small-amplitude librational motions scale RDCs of all N-H bonds by $< C_{20}(\Omega_{\mu}) >$, a factor in the range of ca. 0.93 to 0.97. Motions of sites that undergo additional larger-amplitude motions experience further reductions in their RDCs, as depicted in Fig. 4. The amplitudes of N-H internal motions on timescales less than ca. 1ms can be characterized quantitatively by analysis of RDC data obtained in multiple independent alignment media [54–56]. The alignment tensor has five elements and can be thought of as a five-dimensional vector, which implies that five independent (ideally orthogonal) alignments are optimal. The maximum information is provided by RDCs measured for many N-H bonds, in alignments that span the five-dimensional space [54–58]. In this case it is, in principle, possible to determine the five order parameters of each alignment tensor and of each $<T^{\mu}j>$.

2.4 Biomolecular motions and spin relaxation

Although rapid rotational diffusion in solution causes $< \omega_{\lambda}>$ to vanish in first order, a second-order calculation reveals a small dynamic frequency shift [1]. More importantly, the second-order calculation shows that temporal fluctuations of H_λ can be a potent mechanism for spin relaxation. Spin-relaxation rates are calculated using the semi-classical Hamiltonian of Eq. (4) and second-order time-dependent perturbation theory to solve the equation of motion for the density matrix [1, 9, 21, 23, 24].

2.4.1 The heteronuclear dipolar relaxation mechanism—Theory [1, 21–24] shows that relaxation rates are proportional to spectral densities, $J_m(\omega)$, which are Fourier transforms of correlation functions. For example, the longitudinal autorelaxation rate, R_{1S}, for a spin $S = 1/2$ relaxed by dipolar interaction with a spin $I = 1/2$, is given by [23, 36]

$$R_{IS}=(\omega_D/2)^2\left[J_0(\omega_I-\omega_S)+3J_1(\omega_S)+6J_2(\omega_1+\omega_2)\right] \text{ where, } J_m(\omega)=2\int_0^\infty f_m^D(t)\cos(\omega t)dt \quad (21)$$

$f_m^D(t)$ is an autocorrelation function given by [23, 36]

$$f_m^D(t)=\left\langle R_{2m}^{D*}(0)R_{2m}^D(t)\right\rangle/(\rho_{20}^D)^2 \quad (22)$$

where, R_{2m}^D is defined in Eq. (2) and < > represents an ensemble average. Using Eq. (3),

$$f_m^D(t)=\sum_{q,q'=-2}^{2}\left\langle D_{qm}^{2*}(\Omega_{ML}(0))D_{q'm}^2(\Omega_{ML}(t))D_{0q}^{2*}(\Omega_{PM}(0))D_{0q'}^2(\Omega_{PM}(t))\right\rangle \quad (22)$$

Expressing $f^D_m(t)$ in terms of polar angles $\Omega_B = (\theta_B,\varphi_B)$ and $\Omega\mu = (\theta_\mu,\varphi_\mu)$, shown in Fig. 2, and noting that $D^2_{0q}(\alpha_{PM},\beta_{PM},\gamma_{PM}) = C_{2q}(\theta_\mu,\varphi_\mu)$ yields,

$$\begin{aligned}
&f_m^D(t)=\sum_{q,q'=-2}^{2}\langle f_B(t)f_\mu(t)\rangle\\
&\quad where\\
&\quad f_B(t)=d_{mq}^2(\theta_B(0))\mathrm{e}^{iq\phi_B(0)}d_{mq'}^2(\theta_B(t))\mathrm{e}^{-iq'\phi_B(t)}e^{im(\gamma_{ML}(0)-\gamma_{ML}(t))}\\
&\quad f_\mu(t)=C_{2q}^*(\Omega_\mu(0))C_{2q'}(\Omega_\mu(t))
\end{aligned} \quad (24)$$

and the d^2_{pq} are reduced Wigner matrix elements [26]. Note that $f_\mu(t)$ is independent of α_{PM} (because ρ^D is axially symmetric), while $f_B(t)$ depends upon Euler angle γ_{ML}. This is the angle made by the Y_L axis and the normal to the plane containing the Z_L and Z_M axes.

2.4.2 Spin relaxation in solution—When a biomolecule has a well-defined structure, its overall motion is described by rigid-body rotational diffusion. In the presence of both isotropic overall diffusion and local internal motion, both f_B and f_μ depend upon time; and further, provided these motions are independent, the correlation functions in Eq. (24) can be averaged independently [38, 59] and Eq. (24) written as

$$f_m^D(t)=\sum_{q,q'=-2}^{2}\langle f_B(t)\rangle\langle f_\mu(t)\rangle \quad (25)$$

If the diffusion tensor of the macromolecule is axially symmetric

$$\langle f_B(t)\rangle = (1/5)\delta_{qq'}\exp\{-[6D_\perp + q^2(D_\parallel - D_\perp)]t\} \quad (26)$$

where $D_\parallel$ and $D_\perp$ are the diffusion coefficients for rotations about axes that are parallel and perpendicular to the symmetry axis of the diffusion tensor, respectively [60–62]. Note that, because $<f_B(t)>$ is independent of m, so is f^D. This is a general result that applies to rotational diffusion of an asymmetric rotor in an isotropic liquid [63]. Note that provided $D_\parallel = D_\perp = D_0$, i.e., when the rotor is spherical, $f^D(t)$ is a product of correlation functions for overall and internal motions

$$f^D(t) = (1/5)\exp(-6D_0 t)\left\langle \sum_{q=-2}^{2} C^*_{2q}(\Omega_\mu(0))C_{2q}(\Omega_\mu(t))\right\rangle \quad (27)$$

The addition theorem of spherical harmonics [26] then yields [38]

$$f^D(t) = (1/5)\exp(-6D_0 t)\,\langle P_2(\mu(0)\bullet\mu(t))\rangle \quad (28)$$

Two approaches have been used to evaluate the internal correlation function. In the first, the ensemble average is evaluated using a model for internal motions such as wobbling-in-a-cone, or jumps or diffusion about one or multiple axes [59, 60, 62, 64]. A problem with this approach is that there are usually different motional models that can fit the data. In an alternative “model-free” (MF) approach, an internal correlation function is obtained without explicitly assuming a motional model [38, 65]. Rather, the internal correlation function is approximated as an exponential that decays with a single effective correlation time, τ_e, from its initial value of unity to a plateau of S^2, where S^2 is the generalized order parameter. In the case of isotropic rotational diffusion and an axially symmetric spin Hamiltonian such as H_D, the MF expression for J(ω) is

$$J(\omega) = (2/5)[S^2\tau_c/(1+\omega^2\tau_c^2) + (1-S^2)\tau/(1+\omega^2\tau^2)]\ S^2 = \sum_{q=-2}^{2}|\langle C_{2q}(\theta_\mu,\phi_\mu)\rangle|^2; 1/\tau = 1/\tau_c + 1/\tau_e \quad (29)$$

where, $\tau_c = 1/6D_0$ is the overall correlation time and the angular brackets denote an average over orientations of **μ** on a timescale shorter than approximately τ_c [38]. The MF expression is exact when overall motion is isotropic, $\omega^2\tau_e^2 << 1$, and internal and overall motions are uncoupled. The MF expression for J(ω) remains a good approximation outside its strict range of applicability [66, 67] and has been widely applied to characterize dynamics of biomolecules using measurements of relaxation rates. In a typical application, R_1, $R_{1\rho}$ and the NOE are measured at ^{15}N labeled sites throughout a biomolecule, ideally at several external field strengths, and a MF analysis is used to obtain τ_c, τ_e and S^2. The latter is a model-independent measure of the angular amplitude of the motion of **μ** on a timescale less than τ_c, and can be compared with S^2 predicted by an orientational distribution function $p_{eq}(\Omega_\mu)$ obtained from a motional model or from molecular dynamics simulations. The value of τ_e obtained from the MF analysis provides an estimate of the timescale of the internal motion. A more quantitative interpretation is precluded by the fact that τ_e is a combination of geometric factors and correlation times [38]. A generalization of the MF approach, the extended model free [68] (EMF) approach, has been widely applied to analyze data obtained for biomolecules in which internal dynamics occur on two distinctly different timescales.

The relative ease with which the MF approach yields dynamic information has led to its near-universal use to analyze relaxation data of biomolecules. Physical interpretation of MF parameters requires caution, however, when conditions clearly violate its assumptions; when diffusion of a macromolecule is highly anisotropic ($D_{\|} >> D_{\perp}$), when the spin-interaction tensors are asymmetric, when $\tau_c \approx \tau_e$ or when the overall and internal motions are strongly coupled. Formulations that treat the coupling of overall and internal motions have been developed [13, 69–71].

2.4.3 Spin relaxation in solids—The correlation function given in Eq. (24) is also applicable to spin relaxation in the solid state. In a solid, overall motion of the biomolecule is absent and the orientation of $\boldsymbol{\mu}_B$ is time independent in the M-frame, which we fix in the biomolecule. The correlation function is given by

$$f_m^D(t) = \sum_{q,q'=-2}^{2} f_B(\theta_B, \phi_B) \langle f_\mu(t) \rangle \quad (30)$$

where f_B and f_μ are defined in Eq. (24). Note that in a solid f_B depends only on polar angles (θ_B,φ_B), because γ_{LM} is independent of time and the factor involving this angle in Eq. (24) equals unity. Although (θ_B,φ_B) are also independent of time, they do vary in an un-oriented solid, because $\boldsymbol{\mu}_B$ has a random distribution of orientations in the M-frame, and relaxation rates are orientation dependent. Also, as discussed previously, the resonance frequency is orientation-dependent, making possible direct measurement of the relaxation anisotropy [72] in a non-spinning solid. Such measurements are a powerful means to discriminate among competing models of internal dynamics. However, the broad linewidths observed in non-spinning solids limits such studies to small molecules labeled at single sites. As noted earlier, MAS combined with multidimensional NMR yields liquid-like spectra of solids in which signals of large biomolecules are well resolved and can be assigned with atomic resolution. MAS removes the orientation-dependence of the resonance frequency (and does not affect relaxation rates so long as the spinning rate is much less than the reciprocal of the rotational correlation time), but relaxation rates (R_1, $R_{1\rho}$) are multi-exponential because the observed signal is the superposition of spectral lines from sites fixed in the M-frame, a frame in which B_0 is randomly oriented. In the presence of MAS, R_1 can be calculated using a correlation function [73] that is the sample spinning analogue of Eq. (11). When this correlation function is averaged over all orientations of the spinning axis in the M-frame one finds [73]

$$\overline{f}_m^D(t) = \langle P_2(\mu(0) \bullet \mu(t)) \rangle / 5 \quad (31)$$

This correlation function is orientation-independent. The initial slope of the R_1 relaxation function (which is multi-exponential) is equal to the average R_1 calculated using this correlation function. The latter is formally identical to the correlation function obtained in a liquid, Eq. (28), with D_0 equal to zero. Numeral simulations of powder averaged R_1 and $R_{1\rho}$ rates in spinning solids show that the autocorrelation function decays nearly as a single exponential in the case of either wobbling-in-a-cone or the two-site jump model [74]. This result indicates the MF approach can reasonably be applied to relaxation data of spinning solids.

In a solid sample, $6D_0 = 1/\tau_c = 0$, and the first term of the MF spectral density function, Eq. (29), vanishes, so that relaxation is completely determined by internal motions. This means that relaxation rates of biomolecules measured in the solid state can provide information about internal motion on timescales ranging from approximately 10^{-12} to 10^{-6} s, about two orders of magnitude greater than in solution.

2.4.4 Chemical shift and quadrupolar relaxation mechanisms—At field strengths used to study biomolecules, the ^{15}N CSA and ^{15}N-^{1}H dipolar interaction strengths are comparable. In addition, the amide ^{15}N CSA tensor is nearly axially symmetric, with its symmetry axis nearly parallel to the N-H bond. Depending upon the proton spin state, the two interactions add or subtract, leading to large interference effects arising from cross-correlated relaxation [27]. Werbelow and Grant [61] and Goldman [27] provide theoretical treatments of spin relaxation in the presence of D/D and D/CS cross-correlations, respectively. In order to simplify interpretation of relaxation data, pulse sequences are often employed that suppress D/CS interference when measuring ^{15}N relaxation rates [9].

In general the CS interaction is asymmetric and its angular dependence is expressed using Wigner rotation matrix elements [22, 23]. An asymmetric tensor can be written as the sum of two symmetric tensors [27], and the angular dependence of each tensor can be expressed in terms of spherical harmonics. This simplification is offset by the need to include terms arising from the relaxation interference of the two symmetric tensor interactions [27].

When a deuteron is bound to a carbon atom, the Q interaction is axially symmetric, and the Q interaction tensor has the same angular dependence as the I-S dipolar tensor, Table 1. Therefore the MF approach can be used to analyze ^{2}H relaxation data. Expressions for ^{2}H relaxation rates [75, 76] have the same form as Eq. (3), but differ in detail because the spin operators in the Q and D Hamiltonians differ, Table 1. One of the advantages of deuterium measurements is that, to an excellent approximation, the Q interaction is the sole relaxation mechanism, and, relaxation rates of five different populations and coherences can be measured [76, 77]. ^{2}H relaxation measurements are particularly useful for studies of dynamics of methyl groups [78], whose rapid rotation greatly diminishes the rate of transverse ^{2}H relaxation.

3. Experimental background

3.1 Isotopic enrichment of biomolecules

Contemporary studies of biomolecular dynamics are performed on samples that are labeled with ^{2}H, ^{13}C and/or ^{15}N. The large variety of methods that are now available to label biomolecules has been documented in a recent comprehensive review [79]. The availability of such labeled samples in combination with multidimensional heteronuclear NMR experiments in both solution and solid state have provided extensive signal assignments of many proteins and nucleic acids. These in turn have stimulated the development of multidimensional heteronuclear NMR experiments that provide information about protein dynamics on a wide range of timescales at atomic resolution.

3.2 Measurement of static spin-interaction tensors

In order to derive information about dynamics from measurements of residual anisotropic interactions or relaxation rates, the ‘static’ tensor interaction strengths ω_λ with $\lambda = D, CS, Q$ [11], asymmetry parameters (in the case of CS), and orientations are needed. Recent measurements of RDCs and residual quadrupolar couplings (RQCs), and residual chemical shift anisotropy (RCSAs) in solution, together with measurements of chemical shift tensors in solids, have provided accurate values of these parameters, and their site-to-site variations, in both proteins and nucleic acids [30, 80–94].

3.3 Measurement of residual spin interactions in solution and solid state

Robust methods for measuring RDCs in solution have been available for over a decade [40, 41, 45, 95]. As a consequence of weak alignment, an RDC is usually observed as a small perturbation of the much larger one-bond J coupling, which allows both the sign and the magnitude of the RDC to be readily measured [41]. Two recent advances in methodology are (1) ARTSY [96, 97], which takes full advantage of the TROSY effect to increase the accuracy of measurements of RDCs of large biomolecules, and (2) the use of band-selective homonuclear decoupling to improve resolution and sensitivity of the ^{15}N-^{1}H spectral region in strongly aligned samples [98].

RCSA measurements are more challenging than RDC measurements, because the chemical shift tensor is highly sensitive to the environment and one must minimize environmental perturbations to accurately measure the small differences between isotropic chemical shifts and chemical shifts in weakly aligned samples. Two approaches, the first employing MAS [92], and the second using a specially modified NMR tube [99], have been developed to overcome this problem. In contrast with the widespread measurements of RDCs and RCSAs, measurements of RQCs are rare [82], because of rapid transverse ^{2}H relaxation in biomolecules.

Direct measurements of powder lineshapes in static solids have been used for more than forty years to characterize molecular dynamics in solids [23, 100]. Although solid state spectra of biomolecules are usually acquired using MAS, the information contained in the powder lineshape can be recovered using recoupling techniques. Numerous dipolar recoupling sequences have been used to measure the one-bond heteronuclear dipolar coupling in solids [32–34, 101]. The accuracy of these experiments has been critically examined, particular attention being paid to systematic errors introduced by homonuclear dipolar couplings, RF inhomogeneity, RF calibration errors, and chemical shift offsets. It was concluded [14, 101] that a REDOR [31] recoupling scheme gives the lowest systematic errors for deuterated samples spinning at high MAS frequencies, while the T-MREV [102] sequence gives accurate results in protonated samples spinning at low or intermediate MAS rates. Recently, REDOR has been used to measure order parameters of ^{15}N amide sites [14] and ^{13}C backbone and sidechain sites [103] throughout deuterated crystalline proteins.

As with dipolar couplings, chemical shift tensors have been determined in spinning samples using various approaches, most directly from measurement of side band intensities in spectra acquired at low MAS spinning frequencies [30]. At high spinning frequencies, various approaches have been developed, termed CSA enhancement/amplification in the literature [104, 105], that result in sideband intensities that are the same as when the spinning rate is reduced or the CSA magnitude is amplified. While experiments that measure residual CSA tensors at assigned ^{15}N sites can, in principle, be used to study biomolecular dynamics, such studies have yet to appear, because of uncertainties in rigid-limit CSAs, due to the dependence of CSAs on secondary structure and environment.

3.4 Measurement of relaxation rates in solution and solid state

The first proton-detected relaxation measurements of ^{13}C or ^{15}N spins at sequentially assigned sites throughout proteins in solution were carried out about 25 years ago [106, 107]. Since that time, many refinements have been incorporated into the experiments to reduce systematic errors [9, 108, 109], with recent attention given to minimizing errors in experiments employing TROSY detection in deuterated proteins [110, 111]. With proper care, ^{15}N relaxation rates can be measured with systematic errors of less than a few percent.

Information about biomolecular dynamics has come from widespread measurements of ^{15}N relaxation rates [9, 108, 109] supplemented by less frequent measurements of ^{13}C relaxation rates [9, 112–115]. In uniformly ^{13}C labeled biomolecules, care must be taken with measurement and interpretation of ^{13}C relaxation rates to account for homonuclear couplings, contributions from both dipole-dipole and CSA relaxation mechanisms, and CSA tensors that have often large asymmetries [9, 108, 112, 116, 117]. Studies of protein sidechain dynamics have concentrated on methyl sites. Typically ^{2}H [76, 118] and ^{13}C [119] relaxation in $^{13}C^{1}H_2\,^{2}H$ and $^{13}C^{1}H^{2}H_2$ methyl isotopomers, respectively, have been measured to circumvent complications in interpreting the data caused by cross-correlated dipole-dipole relaxation. Recently, measurements of methyl relaxation rates have been extended to very large proteins (up to 900 kDa) by combining methyl TROSY with various isotope enrichment strategies [94, 120].

Early measurements of ^{15}N relaxation rates at specific sites in crystalline staphylococcal nuclease [121] were limited to R_1 measurements of samples in which a single type of amino acid was ^{15}N labeled. In 2004, Giraud et al. [122] measured $R_1(^{15}N)$ rates at sequentially assigned sites throughout crystalline $^{13}C/^{15}N$ labeled Crh. The number of solid-state measurements of ^{13}C and ^{15}N relaxation rates at individual sites throughout uniformly labeled proteins has increased rapidly since that time [16]. As in solution, pulse sequences have been developed to measure R_1, $R_{1\rho}$, and heteronuclear NOEs [19]; however, in solids particular care must be taken to minimize coherent effects (e.g. proton-driven spin diffusion) [16] on relaxation rates. Such effects are greatly reduced by high-speed MAS ($\upsilon_r > 40$ kHz), particularly when accompanied by dilution of protons by deuterons. Using this approach, R_1 values have been measured for ^{13}C sites throughout crystalline α-spectrin SH3 [103]. In addition, the optimal combination of deuteration and high-speed MAS reduced proton linewidths to about 50 Hz, permitting proton-detected spectra to be recorded with high sensitivity and resolution [103]. Recently it has been shown that inclusion of order parameters, obtained from measurements of dipolar couplings, into a MF analysis greatly improves the accuracy of the amplitudes and timescales derived from solid-state relaxation data [14]. One anticipates that studies of dynamics in solid biomolecules will see rapid growth with continuing advances in solid-state NMR methodology, labeling approaches and sample preparation [123, 124].

4. NMR studies of the dynamics of biomolecular conformational ensembles

4.1 General considerations

In order to relate structural fluctuations to function, it is necessary to characterize their timescales. This is a formidable challenge that requires the determination of an immense number of variables. We shall review recent work on proteins and nucleic acids that addresses this problem by augmenting extensive NMR measurements with state-of-the-art computational approaches.

4.2 Ubiquitin

Ubiquitin is a small (76 amino acids) regulatory protein that functions by binding to a large repertory of target proteins. Analysis of ubiquitin ^{15}N relaxation (R_1, R_2 and NOE) data have shown that significant dynamics on the ps-ns timescale ($S^2 < 0.8$) is confined to loop residues 8–11 and a few residues in other loops [114, 125]. Relaxation dispersion data indicate that dynamics on the ms timescale is limited to residues 23, 25, 55 and 70 [126]. However, the ensemble of crystal structures of ubiquitin bound to a variety of target molecules includes conformations that might lie outside those indicated by relaxation data of the *apo* protein. This observation suggests that, in solution, the *apo* protein may sample conformations on the ns-μs timescale (to which relaxation measurements are insensitive) that encompass those of target-bound ubiquitin and thereby facilitate binding to multiple targets.

In order to test this hypothesis, RDCs of ubiquitin have been measured in both solution and solid state. As noted in the theory section, analysis of RDC measurements that span the five-dimensional alignment space in solution can provide order parameters that contain information about $p_{eq}(\Omega_{\mu i})$ the probability distribution characterizing the ensemble of conformation sampled by each N-H bond orientation. The first application along these lines was made using a model-free RDC approach [54] (MFRDC) to analyze 11 RDC data sets [56]. For many residues, the N-H S^2_{MFRDC} values obtained from this analysis were significantly smaller than S^2 values obtained from a MF analysis of relaxation data in solution. This observation indicated a significant amount of ns-μs timescale dynamics in numerous backbone sites in ubiquitin. Subsequently, the MFRDC analysis was repeated for a greatly expanded data set consisting of RDCs measured in 31 alignments [127]. The average S^2 increased slightly over that found in the original study of 11 data sets, but remained significantly smaller than obtained from relaxation in solution. A modification the MFRDC analysis used an iterative procedure (SCRM) to minimize potential errors introduced by structural bias or noise [128]. Application of the SCRM approach to two large RDC data sets, chosen to best span the alignment space, yielded an average S^2 value of 0.72, compared with 0.78 obtained from relaxation in solution. This result was subsequently enforced by an analysis in which the Gaussian axial fluctuation (GAF) model of peptide plane motion was used to determine the absolute magnitudes of the S^2 values [129]. In accord with these results, $C_\alpha H$ dipolar order parameters derived for crystalline ubiquitin were found to be smaller than those obtained from relaxation in solution [130], presumably as a consequence of motions on the ns-μs timescale.

Taken together, the above results indicate that the backbone of ubiquitin samples an ensemble of molecular structures. In order to obtain insights into function, an all-atom ensemble of ubiquitin structures, 2K39, was generated using MD simulations restrained by NOESY data and by RDCs obtained from more than forty data sets [131]. As cross validation, the ensemble was virtually unchanged when it was generated using the RDCs alone, and the S^2 values of 2K39 were in agreement, within experimental error, with those derived from the SCRM analysis [128]. Additionally, it was found that the 2K39 ensemble encompassed the structural heterogeneity observed in 46 ubiquitin crystal structures, in most of which ubiquitin is bound to a target protein. Based on this observation it was concluded that conformational selection, rather than induced fit, suffices to explain the molecular recognition dynamics of ubiquitin. This work was extended to study correlated motions in ubiquitin by combining measurements of cross-correlated relaxation rates ($R_{NH,NH}$) and ($R_{NH,C\alpha H\alpha}$) and trans-hydrogen bond scalar couplings ($^{3h}J_{NC'}$) with RDC data [50] to generate an ensemble 2KOX. 2KOX yielded better agreement with the combined data sets than did 1D3Z (the average NMR structure in solution), 1UBQ (the X-ray structure of free ubiquitin) or the 2K39 ensemble. Analysis of the 2KOX ensemble indicated that concerted motions, mediated by the hydrogen-bond network that connects four β-strands of ubiquitin, link target recognition sites of the protein.

While the ensembles derived from these comprehensive analyses of the extensive RDC data provide an attractive explanation of how ubiquitin dynamics relates to function, other investigations have cast doubt about the extent of flexibility indicated by this work. An ensemble simulated annealing approach, developed by Clore and Schwieters [132] showed that an ensemble consisting of only two members accounted for 17 sets of RDCs of N-H, N-C', H_N-C′ and C_α-C′ vectors in ubiquitin measured in multiple alignment media. Except for a few residues, mostly in loops, S^2 values exceeded 0.8. In an alternative approach [133], accelerated MD (AMD) simulations were used to vary the level of conformational sampling and thereby access dynamics over a wide range of time scales. The optimized AMD acceleration level was determined by best-fitting N-H RDCs obtained in 23 alignments. S^2 values were determined for the corresponding ensemble, and although they were less than S^2 obtained from relaxation data in several loops, they were not as small as S^2 obtained in the SCRM and GAF analyses.

Recent experimental results, obtained for ubiquitin in solution and solid state, also indicate that motions on the ns-μs timescale may be less extensive than indicated by the analyses of RDC data in solution. Analysis of recent measurements of N-H dipolar couplings in crystalline ubiquitin [14] yield S^2 values in close agreement with those obtained from relaxation measurements in solution, Fig. 5A. Furthermore, although dipolar couplings measured in solution and solid state are both sensitive to motions on the ns-μs timescale, the S^2 values obtained from analysis of RDCs in the solid state [14] differ significantly from analysis of RDCs obtained in solution [129], Fig. 5B. Although there is some uncertainty regarding the scale factor to be used when deriving order parameters from RDC data, it is clear from Fig. 5B that the discrepancy cannot be removed by scaling either set of order parameters. (Problems associated with the scaling factors to be applied when comparing S^2 from various types of solution- and solid-state RDC measurements are discussed in the literature [14, 58, 129, 134]). One possible interpretation of the results in Fig. 5 is that small amplitude motions of ubiquitin on the ps-ns timescale are of similar amplitude in solution and solid state, while larger amplitude motions that occur in solution on the ns-μs timescale are quenched by intermolecular contacts in the crystalline state.

Unfortunately this plausible explanation does not appear to be supported by two recent studies. In the first [135], new RDCs were measured in squalamine (in which ubiquitin alignment is significantly different from most alignment media used in previous studies) as well as Pf1. These data, together with all experimental restraints previously used to derive the NMR structure, 1D3Z, were used to obtain a new average NMR structure, 2MJB. In order to assess and validate the quality of this structure, ^{13}C' RCSAs, $C_\alpha C_\beta$ RDCs and $^3J_{HNH\alpha}$ scalar couplings were measured. These data, which were not used in any previous studies, were also used to validate the 2KOX and an X-ray-derived ensemble. Table 2 lists validation statistics of 2MJB, along with those of the 2KOX and the X-ray ensemble. The results show that the single NMR structure and an ensemble of the 15 highest resolution X-ray structures predict the validation parameters for the most-ordered residues better than does the 2KOX ensemble. While this is reasonable, it is surprising that even for the 13 most mobile residues in ubiquitin, the 2KOX statistics are no better than those of either the single NMR structure or the narrow distribution of structures that comprise the X-ray ensemble. Fig. 6 shows representations of the backbone structures of the 2KOX and X-ray ensembles, overlaid on the average NMR structure, 2MJB. It is clear that the X-ray ensemble samples considerably less conformation space than does 2KOX, and has slightly superior validation statistics.

In a second study [136], the structures of five proteins were refined against both high resolution X-ray diffraction data and NMR (PCS and RDC) data. The purpose of this investigation was to test whether a single structure could fit both types of data to within experimental error. In the case of ubiquitin it was found that a single structure, in which only a few dynamic residues were excluded, provided an excellent fit to both the X-ray data (PDB 3nhe) as well as the set of 36 RDCs measured by Lange et al. [131]. It therefore seems that the answer to the question, “Just how dynamic is ubiquitin on the ns-μs timescale?” awaits further research.

4.2 Calmodulin

Calmodulin (CaM) is a calcium-sensing protein that regulates many cellular regulatory processes in a Ca^{2+}-dependent manner by binding to a wide array of target molecules. In the crystalline state, fully calcium-loaded CaM ($4Ca^{2+}$CaM) typically adopts a dumbbell-shape in which two globular domains, each bound to two Ca^{2+} ions, are connected by a long α-helix [137–139], Fig. 7. While the X-ray work revealed the interactions between the bound Ca^{2+} ions and the protein, the crystal structure did not indicate how $4Ca^{2+}$CaM is able to bind to numerous different target molecules. X-ray scattering suggested that the central helix is flexible in solution and a MF analysis of ^{15}N spin relaxation measurements [140] identified residues in the center of the helix that are flexible on the subnanosecond timescale, based upon their reduced order parameters. This observation indicated that a flexible hinge in the central helix facilitates target binding, a finding that was confirmed by subsequent NMR and crystal structures of 4Ca^{2+}CaM bound to target molecules [141, 142]. In each structure of target-bound 4Ca^{2+}CaM, the protein adopts a compact conformation in which the angle between the axes of the N- and C-terminal halves of the central helix is about 90°.

4Ca^{2+}CaM serves as a model of a large class of flexible multi-domain proteins that function by adopting multiple conformations that are thought to facilitate binding to a variety of target molecules. Therefore, numerous NMR studies have been directed at learning about the timescale of 4Ca^{2+}CaM domain dynamics as well the angular distributions of domain orientations. In an early effort to obtain this information, N-H sites that are sensitive to reorientation of the N- and C-terminal central helix axes, but are insensitive to rotations about these axes, were included in a MF analysis of ^{15}N relaxation data acquired at three field strengths [143]. It was found that the two domains executed wobbling motions with correlation times of about 3 ns and order parameters in the range 0.62–0.74. If one assumes that the central helix axes of N- and C-terminal domains diffuse uniformly in a cone, the cone semi-angles derived from the order parameters are found to be about 30°, Fig. 7.

While the amplitude of the domain reorientation indicated by the MF analysis is significant, in structures of 4Ca^{2+}CaM bound to peptide targets, the central helix bends by at least 90° [144]. If one assumes that the distribution of orientations in the cone is not uniform, but decreases as the cone angle increases (e.g., as for a Gaussian distribution), then the order parameters are compatible with orientational distributions having a small but non-zero probability for cone angles greater than 90°.

Two limitations to using the MF analysis of relaxation data to elucidate the motions of the N- and C-terminal domains of 4Ca^{2+}CaM are (1) the coupling of overall and domain motions is neglected and (2) the relaxation data are insensitive to motions having correlation times greater than about 10 ns. Bertini et al. [46] have developed a clever approach to circumvent these shortcomings. They began with the demonstration that the N60D mutant of 4Ca^{2+}CaM selectively binds a lanthanide (Ln) exclusively at a single site in the N-terminal domain (the site-II Ca^{2+} binding location), and can only bind Ca^{2+} at the other three binding sites. Using this mutant, various 3Ca^{2+}LnCaM derivatives were prepared. The N-terminal domain experiences weak magnetic alignment as a consequence of the anisotropic susceptibility tensor, χ, of the bound lanthanide, allowing PCSs and RDCs to be measured.

The alignment tensor of the N-terminal domain was obtained from the PCS data and that of the C-terminal domain was obtained from the RDC data. The alignment tensors of the two domains would be identical if the linker connecting them adopted a single conformation. Otherwise, the span of RDCs of the C-terminal domain will be less than that of the N-terminal domain as a consequence of inter-domain dynamics [145]. This is evident if one takes the perspective of an observer in the C-terminal domain. In this domain, the orientation of the χ-tensor samples a distribution of orientations, resulting in averaging of the χ-tensor and the RDCs of sites in the C-terminal domain.

Although the PCS and RDC data provide the orientations of the principal axes of the alignment tensor in each domain, the PAS orientations are not unique but are subject to a well-known four-fold degeneracy [40]. This limits the unambiguous information that can be obtained about ensembles sampled by the two domains. This problem is greatly reduced by recording data of three $3Ca^{2+}$LnCaM constructs, where Ln = Tb^{3+}, Tm^{3+}, Dy^{3+}, are lanthanides whose χ-tensor orientations differ [146, 147]. The PCS and RDC data, supplemented with SAXS data, were used to estimate the maximum occurrence (MO) of the conformations sampled by $3Ca^{2+}$LnCaM. The MO approach, described in detail in the original publication [147], indicated that the fully and partially extended states of $3Ca^{2+}$LnCaM had MOs of 15% and 35% respectively. While these measurements provide strong evidence that the extended states dominate the conformational ensemble, the 5% MO of the most compact states, similar to those seen in crystal structures of target-bound $4Ca^{2+}$CaM, leaves open the possibility that a small percentage of $3Ca^{2+}$LnCaM conformations sample target-bound conformations.

Direct evidence for the presence of a small population of compact $4Ca^{2+}$CaM states was obtained from amide proton paramagnetic relaxation enhancement (PRE) data [148]. The advantage of PRE measurements is that the contribution of an inter-domain PRE of an amide proton of a compact state, in which the spin label in one domain comes close to the amide proton site in the other domain, is greatly magnified by the $<r^{-6}>$ dependence of the PRE. Two $4Ca^{2+}$CaM constructs, each containing a single cysteine point-mutation in the N- and C-terminal domains, S17C and S128C, respectively, were labeled with a paramagnetic nitroxide spin label [148]. Transverse PREs were measured for amide sites throughout both constructs. Analysis of the PRE data yielded an ensemble of $4Ca^{2+}$CaM conformations containing about 10% compact structures, about one-half of which resembled the conformation(s) observed in X-ray structures of target-bound $4Ca^{2+}$CaM.

Independently, PRE measurements of transverse relaxation of amide protons were made [149] on $3Ca^{2+}Gd^{3+}$CaM where a gadolinium ion replaces the Ca^{2+} at the II-binding-site of the N60D construct. An MO analysis was then applied to the PRE data combined with the PCS and RDC data acquired previously [149]. The two types of data are complementary, and their combination yielded a better definition of the MOs of both extended and compact conformations than was the case when only one type of data was used. Using the pooled data, the MO of the highly compact states increased to 20%, as compared with the MO of 5% obtained in the absence of PRE data. This result is consistent with the analysis of the spin-labelled data, where approximately 10% of the conformations in the $4Ca^{2+}$CaM ensemble are highly compact structures.

A different approach, using chemical shifts as replica-averaged restrains in MD simulations, has recently been used to characterize domain motions of $4Ca^{2+}$CaM [144]. The chemical shifts of ten residues in the central helix, whose conformations differ in the extended (unbound) and compact (target–bound) states were used as restraints in MD calculations that generated an ensemble of $4Ca^{2+}$CaM conformations. The ensemble was validated by its ability to predict RDC, PRE and SAXS data. The polar coordinate system depicted in Fig. 8A was introduced in order to compare the ensembles obtained by various investigators. The use of polar angles (rather than Euler angles) does not permit one to discriminate conformations that differ by rotations around the axis of helix V (shown in orange in Fig. 8A), but it does facilitate visual comparisons of ensembles obtained by various investigators. The fully extended X-ray conformation corresponds to polar angles (θ, φ) = (90°, 0°), while the polar angles of the target-bound $4Ca^{2+}$CaM structures all cluster in the region (green circle) centered at (θ, φ) = (10°, 110°), Fig 8(B) [144]. The chemical shift and spin-labelled PRE ensembles are displayed in yellow-red scales and grey scales, respectively. In agreement with the analysis of relaxation and PCS/RDC data [146, 147], most conformations based on the chemical shift distribution have (θ, φ) values within 45° of the fully extended X-ray structure. Compact structures, with coordinates approaching those obtained from X-ray structures of target-bound $4Ca^{2+}$CaM, are found with much lower probability, in agreement with conclusions obtained from analyses of PRE data [148, 149]. It is noteworthy that, while the coordinates of these compact states approach those of target-bound $4Ca^{2+}$CaM, they differ from the latter by at least 40° in both (θ, φ). Therefore it appears that the conformations that $4Ca^{2+}$CaM adopts when bound to target molecules are, in the case of the free protein, only present at levels below the detection limits of available RDC and PRE data, showing that their free energies in the absence of bound target molecules are elevated.

4.4 TAR, the HIV-1 trans-activation response element RNA

Like proteins, nucleic acids often undergo large conformational changes in order to function, and numerous NMR studies have been directed at delineating nucleic acid dynamics in order to better understand their function. Recent reviews [18, 53, 150, 151] have provided excellent overall coverage of this work. Herein I focus on approaches directed at overcoming the particular challenges encountered when using RDC and spin relaxation data for the investigation of the dynamics of TAR.

TAR is a small RNA that is essential for viral replication (structure E0 in Fig. 9A). Early structural NMR and X-ray studies showed that TAR adopted quite different conformations on binding to ligands, metal ions and small molecule inhibitors. In addition, early RDC measurements and MD simulations indicated that TAR was flexible in the free state. The question I should like to address is: “does free TAR sample a range of conformations that includes those observed in the ensemble of bound structures, and if so, on what timescale?”

TAR contains two helical domains of about equal size that are linked by a flexible bulge (see structure E0 of Fig. 9A,) Because the helical stems are nearly of the same size, overall tumbling of TAR is strongly coupled to domain reorientation, which greatly complicates analysis of spin relaxation data [13, 69, 71, 152, 153]. Decoupling of these motions was achieved by elongating the domain I helix of TAR with a stretch of 22 unlabeled A-form Watson-Crick base pairs [154] (structure EI-22 of Fig 9A,) As a consequence of elongation, EI-22-TAR diffuses as an axially symmetric rotor whose overall motion is not significantly affected by the internal motion of the unmodified small domain. Elongation also increases the overall correlation time, which extends the upper limit of the timescale of internal motions reported on by relaxation rates. C-H signal intensities of EI-22-TAR were significantly smaller for residues in the elongated domain I than in domain II, indicating that EI-22-TAR does not diffuse as a rigid body. This interpretation was confirmed by an extended MF analysis of R_1, R_2 and NOE data of imino ^{15}N-H sites which revealed that, in addition to local ps fluctuations of N-H bond axes (S^2 ca. 0.84) experienced in both domains, N-H sites in domain II only experienced slower (τ ca. 1.7 ns) motions with larger amplitudes (S^2 ca. 0.72). Analysis of relaxation data of EI-22-TAR-Arg (TAR bound to argininamide) also showed that Arg binding abolishes inter-domain motions.

The upper limit on the timescale of EI-22-TAR domain motions that can be accessed through measurements of relaxation times is 10–20 ns. In order to extend measurements of domain dynamics to the ns-ms timescale, EI-22-TAR RDCs were measured in a Pf1 alignment medium. The alignment tensor of the EI-22-TAR large domain is axially symmetric, with its unique principal axis parallel to axis of the long helix. As a consequence of inter-domain motion the alignment tensor of the small domain is asymmetric and of smaller magnitude than that of the large domain. As discussed in the theory section, the five elements of the averaged alignment tensor observed in the small domain yield five of the $<C_{2m}>$ coefficients needed to describe the orientational probability distribution of the domain I helix axis relative to the PAS system of the alignment tensor of the small domain. Because the alignment of domain I is axially symmetric, these coefficients do not contain information about the angle that describes twisting of domain I about its long axis. This information is obtained from analysis of RDCs measured on two complementary TAR constructs, structures EI-22 and EII-22 (Fig. 9A), where the long helix is used to elongate either of the helical domains [48]. The generalized order parameter calculated from the analysis of both sets of RDC data was found to be ca. $S^2 = 0.21$, significantly less than the value, of ca. $S^2 = 0.72$, obtained from the analysis of the relaxation data (see above). In addition, no evidence for exchange broadening was obtained for residues either in or near the TAR bulge. Taken together these observations indicate that significant inter-domain dynamics occurs on the ns to μs timescale [48].

Although S^2 provides useful information about the amplitudes of TAR domain motions, it represents the sum of five squared order parameters. In contrast, the RDCs of the two elongated constructs yield nine separate order parameters [155] that provide more information about TAR dynamics. It was found that a minimum of three TAR conformations were required to fit the pooled RDC data [48]. The three TAR conformations (Fig. 9B) spanned large angular amplitudes in a highly directional manner.

A more detailed all-atom representation of TAR dynamics was obtained by applying a sample-and-select approach [156] to a TAR MD simulation of 80 ns [157]. The calculated MD pool of conformations was randomly sampled and each individual conformation was selected for inclusion in the final ensemble based depending on its ability to improve the fit to the TAR RDC data. An ensemble of twenty conformations was found to satisfy the measured RDCs to nearly within experimental uncertainty. This ensemble encompassed the three-state ensemble, depicted in Fig. 9B, and included conformations similar to the ligand-bound conformations of TAR [157].

While the elongation strategy has obvious advantages, it also has its limitations. Not all RNA molecules are amenable to elongation. Furthermore, elongation of two helical domains limits the acquired RDC data to two independent alignments, whereas data need to be acquired in five independent alignment media in order to maximize the information that they contain. A strategy to overcome these limitations was developed based on the observations that extension of TAR by as few as three base pairs or by the introduction of kinks in short-elongation segments significantly modulates alignment [158]. The problem with coupling of overall and domain motions in such constructs was addressed using PALES [159, 160] to calculate the alignment tensor for every conformation sampled by the TAR construct. This approach was justified by studies [161–163] that showed that alignment tensors of several nucleic acids dissolved in Pf1 phage were well predicted by a simple steric model. Although the phage and the RNA molecules are both negatively charged, electrostatic repulsion will mimic steric occlusion when the negative charge distribution of the RNA follows its shape and repels the negatively charged Pf1. Using this approach, the RDC data sets from the four TAR constructs in Fig. 9A and a conformational pool obtained from an 8.2 μs MD trajectory were used together with the sample-and-select scheme [156] to construct a twenty-member ensemble that fitted the RDC data within experimental uncertainty [53, 164]. The ensemble was validated by showing that it could predict RDCs measured for a magnetically aligned TAR sample (not used to construct the ensemble) as well as proton chemical shifts. The RDC ensemble was used to calculate order parameters at specific sites in TAR, which were then compared with order parameters obtained from ^{13}C and ^{15}N relaxation data. Differences in order parameters were then used to distinguish sites that were mobile on the ps-μs timescale from those whose mobility was restricted to the ps-ns timescale. A comprehensive discussion of TAR dynamics obtained from these studies is provided in the original publications [53, 164].

An independent investigation of TAR dynamics has been made by obtaining RDC and relaxation data in solution as well as ^{2}H lineshape and relaxation data of hydrated TAR in the solid state where overall motion is absent. The ^{2}H measurements report on both the rates and amplitudes of domain and local internal motions. Three TAR samples were prepared, [5, 6-^{2}H] labeled at U23, U25 and U38, and ^{2}H lineshapes and R_1 and R_{1Q} relaxation rates were measured as a function of hydration varying from 6 to 30 water molecules per nucleotide [165, 166]. From an analysis of these data it was concluded that TAR experiences slow (ns to μs timescale) domain dynamics, like those observed in solution, when the hydration level is high (sixteen water molecules per nucleotide), corresponding to complete local hydration. Analysis of data acquired at this hydration level showed that residues involved in binding of TAR to Tat (the HIV transcription activating protein) were mobile on the ns-μs timescale, as well as the faster ps-ns timescale found from relaxation measurements in solution.

In a subsequent study [167], detailed models of the dynamics of the three deuterated sites, on the ns-μs timescale, were derived from analysis of ^{2}H lineshapes and R_1, R_{1Q} relaxation data. It was found that U23 and U25 (Fig. 9A) undergo changes in orientation of ca. 30° at a rate of 6–7 × 10^7 s^{-1}, and in addition the base of U25 undergoes a slow (6 × 10^5 s^{-1}) large-amplitude (± 40°) twist. U38 was found to execute 13° twisting and bending motions with a rate of 6 × 10^5 s^{-1}. It was concluded that these large-amplitude motions enabled TAR to sample conformations similar to those observed when it was bound to Tat.

These studies, which focused on analysis of solid-state NMR data, were expanded to include relaxation measurements in solution. In order to do so, an approach was developed to treat the difficult problem of accounting for the coupling of overall and domain motion. In the first instance this was done [168] for data acquired for a single site, U38. This nucleotide had been shown to execute domain-related motions in the solid state at a rate (6×10^5 s^{-1}) much less than the overall diffusion rate (ca. 10^9 s^{-1}) of TAR in solution. Taking advantage of the separation in rates, a slow-exchange model was used to analyze the combined solution-state/solid-state data for U38. This approach was then extended by formulating a more general exchange (GE) theory, which applies for arbitrary rates of overall diffusion and domain motions, on the condition that the orientations of the PASs of the diffusion tensors coincide at the instant of exchange [71, 152]. A more general theory, where this restriction has been removed, has recently been presented by Ryabov et al. [13].

Motional models derived from the combined analysis of solution and solid-state NMR data were discussed and compared [71, 152] with the results obtained by Al-Hashimi et al. [48, 154, 155]. More recently the combined solution/solid-state data have been used to construct an ensemble of TAR structures [169]. In this approach, RDCs were used to filter an initial set of 500 ROSETTA energy-minimized TAR structures, yielding a set of five structures. Next, these five structures were shown to correspond to conformational clusters obtained from a principal component analysis applied to the 500 starting conformations. Finally it was found that applying the GE theory to the five-member ensemble reproduced the ^{13}C-^{1}H relaxation rates measured in solution.

A comparison of the results obtained using the five-member ensemble [169] with those of the twenty-member ensemble [53, 164] revealed excellent agreement in angles spanned by the two helical domains. However, bulge conformations obtained from the two ensembles differed significantly [169]. It is possible that the discrepancy arises from the limited size of the initial pool of energy-minimized structures and/or from the assumption, in the GE theory, of a coincidence of the rotational diffusion tensors at the instant of exchange. Another source of potential error in both approaches is the use of a steric model to calculate alignment tensors of RNA in charged media [170].

5. Perspectives

Until about 15 years ago, NMR studies of biomolecular dynamics typically relied on MF analyses of relaxation measurements to derive order parameters and correlation times of ^{2}H, ^{13}C and ^{15}N sites. Subsequently new methods have provided large amounts of additional data, primarily in the from of RDCs, PCSs and PREs in solution as well as relaxation rates and averaged dipolar couplings in the solid state. This increase in the amount of data available for analysis has been accompanied by an over 1000-fold increase in the duration covered by MD simulations, which now extend to the ms regime. These developments have encouraged investigators to obtain all-atom descriptions of the ensembles of conformations that are sampled by biomolecules on a timescale ranging from ps-ms. The three examples considered herein reveal that significant progress has be made towards achieving this goal, but challenges remain. In the case of ubiquitin, it has been shown that amide backbone motions on ps-ns timescales have nearly identical order parameters in solution and crystalline states; however, the amplitudes of ns-μs timescale motions in solution remain uncertain, as does the question regarding of extent of conformational sampling in solution. Calmodulin and TAR are examples of biomolecules in which two well-structured domains are connected by short flexible linkers, so that domain motions are a function of a relatively small number of degrees of freedom. It is likely that this is one reason that generally good agreement has been obtained by different investigators regarding the nature of domain dynamics for the two molecules. However, calmodulin illustrates the difficulty of detecting biologically important conformations, which have low populations (<1%) even when proton PREs are measured. Detection of such states should be aided by the continued development of novel paramagnetic labels [171, 172] that will increase the range of sites that can be tagged by PRE agents. In addition, an expanded repertoire of paramagnetic tags will provide alignments of biomolecules that complement those provided by liquid crystals and gels, and thereby improve the prospect of attaining five fully independent alignment data sets. Finally, as both the accuracy and speed of MD computations continue to improve, is should be possible to calculate long-time correlation functions and refine ensembles directly against NMR data, and thus avoid the simplifying approximations inherent in MF and other approaches currently used to analyze relaxation data.

Acknowledgements

I thank Ad Bax, Marius Clore, Attila Szabo, Rob Tycko and Jinfa Ying for numerous helpful suggestions. This work was supported by the NIH Intramural Research Programs of the NIDCR and NIDDK.

References

1. Abragam, A. The Principles Of Nuclear Magnetism. Oxford, U.K.: Oxford University Press; 1961.
2. Ernst RR, Anderson WA. Application of Fourier transform spectroscopy to magnetic resonance. Rev. Sci. Instrum. 1966; 37:93–102.
3. Allerhand A, Doddrell D, Glushko U, Cochran DW, Wenkert E, Lawson PJ, Gurd FRN. Carbon-13 Fourier tranform nuclear magnetic resonance .3. Conformation and segmental motion of native and denatured ribonuclease-A in solution - application of natural-abundance carbon-13 partially relaxed Fourier transform nuclear magnetic resonance. J. Am. Chem. Soc. 1971; 93:544–546. [PubMed: 5541522]
4. Oldfield E, Norton RS, Allerhand A. Studies of individual carbon sites of proteins in solution by natural abundance carbon- 13 nuclear magnetic-resonance spectroscopy - relaxation behavior. J. Biol. Chem. 1975; 250:6368–6380. [PubMed: 169239]
5. Wagner G, Demarco A, Wuthrich K. Dynamics of aromatic amino-acid residues in globular conformation of basic pancreatic trypsin-inhibitor (BPTI) .1. H-1 NMR-studies. Biophysics of Structure and Mechanism. 1976; 2:139–158. [PubMed: 9165]
6. Wittebort RJ, Rothgeb TM, Szabo A, Gurd FRN. Aliphatic groups of sperm whale myoglobin - C-13 NMR-study. Proc. Natl. Acad. Sci. USA. 1979; 76:1059–1063. [PubMed: 286293]
7. Richarz R, Nagayama K, Wuthrich K. C-13 nuclear magnetic-resonance relaxation studies of internal mobility of the polypeptide-chain in basic pancreatic trypsin-inhibitor and a selectively reduced analog. Biochemistry. 1980; 19:5189–5196. [PubMed: 6160872]
8. Mollova ET, Pardi A. NMR solution structure determination of RNAs. Curr. Opin. Struct. Biol. 2000; 10:298–302. [PubMed: 10851189]
9. Cavanagh, J.; Fairbrother, WJ.; Palmer, AG.; Rance, M.; Skelton, NJ. Protein NMR Spectroscopy: Principles And Practice. 2nd ed.. San Diego: Academic Press; 2006.

10. Comellas G, Rienstra CM. Protein structure determination by magic-angle spinning solid-state NMR, and insights into the formation, structure, and stability of amyloid fibrils. Annu. Rev. Biophys. Biomol. Struct. 2013; 42:515–536.
11. Torchia DA. Dynamics of biomolecules from picoseconds to seconds at atomic resolution. J. Magn. Reson. 2011; 212:1–10. [PubMed: 21840740]
12. Osawa M, Takeuchi K, Ueda T, Nishida N, Shimada I. Functional dynamics of proteins revealed by solution NMR. Curr. Opin. Struct. Biol. 2012; 22:660–669. [PubMed: 23000032]
13. Ryabov Y, Clore GM, Schwieters CD. Coupling between internal dynamics and rotational diffusion in the presence of exchange between discrete molecular conformations. J. Chem. Phys. 2012; 136:034108. [PubMed: 22280745]
14. Haller JD, Schanda P. Amplitudes and time scales of picosecond-to-microsecond motion in proteins studied by solid-state NMR: A critical evaluation of experimental approaches and application to crystalline ubiquitin. J. Biomol. NMR. 2013; 57:263–280. [PubMed: 24105432]
15. Krushelnitsky A, Reichert D, Saalwachter K. Solid-state NMR approaches to internal dynamics of proteins: From picoseconds to microseconds and seconds. Acc. Chem. Res. 2013; 46:2028–2036. [PubMed: 23875699]
16. Lewandowski JR. Advances in solid-state relaxation methodology for probing site-specific protein dynamics. Acc. Chem. Res. 2013; 46:2018–2027. [PubMed: 23621579]
17. Ortega G, Pons M, Millet O. Protein functional dynamics in multiple timescales as studied by NMR spectroscopy. Dynamics of Proteins and Nucleic Acids. 2013; 92:219–251.
18. Shapiro YE. NMR spectroscopy on domain dynamics in biomacromolecules. Prog. Biophys. Mol. Biol. 2013; 112:58–117. [PubMed: 23684958]
19. Zinkevich T, Chevelkov V, Reif B, Saalwachter K, Krushelnitsky A. Internal protein dynamics on ps to mu s timescales as studied by multi-frequency N-15 solid-state NMR relaxation. J. Biomol. NMR. 2013; 57:219–235. [PubMed: 24048638]
20. Watt ED, Rienstra CM. Recent advances in solid-state nuclear magnetic resonance techniques to quantify biomolecular dynamics. Anal. Chem. 2014; 86:58–64. [PubMed: 24313950]
21. Redfield AG. The theory of relaxation processes. Adv. Magn. Reson. 1965; 1:1–32.
22. Haeberlen, U. High Resolution NMR In Solids. Academic Press: New York; 1976.
23. Spiess HW. Rotation of molecules and nuclear spin relaxation. NMR Basic Principles Prog. 1978; 15:55–214.
24. Ernst, RR.; Bodenhausen, G.; Wokaun, A. Principles of Nuclear Magnetic Resonance in One and Two Dimensions. Oxford: Clarendon Press; 1987.
25. Emsley, JW. Liquid crystals: General considerations. In: Harris, RK.; Wasylishen, RE., editors. Encyclopedia of Nuclear Magnetic Resonance. London: Wiley; 2012. p. 2355-2367.
26. Brink, DM.; Satchler, GR. Angular Momentum. 3rd ed.. London: Oxford University Press; 1994.
27. Goldman M. Interference effects in the relaxation of a pair of unlike spin-1/2 nuclei. J. Magn. Reson. 1984; 60:437–452.
28. Maricq MM, Waugh JS. NMR in rotating solids. J. Chem. Phys. 1979; 70:3300–3316.
29. Herzfeld J, Berger AE. Sideband intensities in NMR: Spectra of samples spining at the magic angle. J. Chem. Phys. 1980; 73:6021–6030.
30. Wylie BJ, Sperling LJ, Frericks HL, Shah GJ, Franks WT, Rienstra CM. Chemical-shift anisotropy measurements of amide and carbonyl resonances in a microcrystalline protein with slow magic-angle spinning NMR spectroscopy. J. Am. Chem. Soc. 2007; 129:5318–5319. [PubMed: 17425317]
31. Gullion T, Schaefer J. Rotational-echo double-resonance NMR. J. Magn. Reson. 1989; 81:196–200.
32. Nielsen NC, Strasso LA, Nielsen AB. Dipolar recoupling. Solid State NMR. 2012; 306:1–45.
33. De Paepe G. Dipolar recoupling in magic angle spinning solid-state nuclear magnetic resonance. Annual Review of Physical Chemistry. 2012; 63:661–684. 63.
34. Bjerring M, Jain S, Paaske B, Vinther JM, Nielsen NC. Designing dipolar recoupling and decoupling experiments for biological solid-state NMR using interleaved continuous wave and rf pulse irradiation. Acc. Chem. Res. 2013; 46:2098–2107. [PubMed: 23557787]

35. Snyder LC. Analysis of nuclear magnetic resonance spectra of molecules in liquid-crystal solvents. J. Chem. Phys. 1965; 43:4041–4050.
36. Torchia DA, Szabo A. The information content of powder lineshapes in the fast motion limit. J. Magn. Reson. 1985; 64:135–141.
37. Moltke S, Grzesiek S. Structural constraints from residual tensorial couplings in high resolution NMR without an explicit term for the alignment tensor. J. Biomol. NMR. 1999; 15:77–82. [PubMed: 20703963]
38. Lipari G, Szabo A. Model-free approach to the interpretation of nuclear magnetic resonance relaxation in macromolecules. 1. Theory and range of validity. J. Am. Chem. Soc. 1982; 104:4546–4559.
39. Saupe A, Englert G. High-resolution nuclear magnetic resonance spectra of orientated molecules. Phys. Rev. Lett. 1963; 11:462–464.
40. Prestegard JH, Al-Hashimi HM, Tolman JR. NMR structures of biomolecules using field oriented media and residual dipolar couplings. Q. Rev. Biophys. 2000; 33:371–424. [PubMed: 11233409]
41. Bax A, Kontaxis G, Tjandra N. Dipolar couplings in macromolecular structure determination. Methods Enzymol. 2001; 339:127–174. [PubMed: 11462810]
42. Tolman JR, Ruan K. NMR residual dipolar couplings as probes of biomolecular dynamics. Chem. Rev. 2006; 106:1720–1736. [PubMed: 16683751]
43. Losonczi JA, Andrec M, Fischer MWF, Prestegard JH. Order matrix analysis of residual dipolar couplings using singular value decomposition. J. Magn. Reson. 1999; 138:334–342. [PubMed: 10341140]
44. Bertini I, Luchinat C, Piccioli M. Paramagnetic probes in metalloproteins. Methods Enzymol. 2001; 339:314–340. [PubMed: 11462819]
45. Kay LE. Nuclear magnetic resonance methods for high molecular weight proteins: A study involving a complex of maltose binding protein and beta-cyclodextrin. Meth. Enzymol. 2001; 339B:174–203. [PubMed: 11462811]
46. Bertini I, Gelis I, Katsaros N, Luchinat C, Provenzani A. Tuning the affinity for lanthanides of calcium binding proteins. Biochemistry. 2003; 42:8011–8021. [PubMed: 12834353]
47. Zhang Q, Al-Hashimi HM. Domain-elongation NMR spectroscopy yields new insights into RNA dynamics and adaptive recognition. RNA-A Publication of the RNA Society. 2009; 15:1941–1948.
48. Zhang Q, Stelzer AC, Fisher CK, Al-Hashimi HM. Visualizing spatially correlated dynamics that directs RNA conformational transitions. Nature. 2007; 450:1263–1267. [PubMed: 18097416]
49. Fisher CK, Zhang Q, Stelzer A, Al-Hashimi HM. Ultrahigh resolution characterization of domain motions and correlations by multialignment and multireference residual dipolar coupling NMR. J. Phys. Chem. B. 2008; 112:16815–16822. [PubMed: 19367865]
50. Fenwick RB, Esteban-Martin S, Richter B, Lee D, Walter KFA, Milovanovic D, Becker S, Lakomek NA, Griesinger C, Salvatella X. Weak long-range correlated motions in a surface patch of ubiquitin involved in molecular recognition. J. Am. Chem. Soc. 2011; 133:10336–10339. [PubMed: 21634390]
51. Deshmukh L, Schwieters CD, Grishaev A, Ghirlando R, Baber JL, Clore GM. Structure and dynamics of full-length HIV-1 capsid protein in solution. J. Am. Chem. Soc. 2013; 135:16133–16147. [PubMed: 24066695]
52. Guerry P, Mollica L, Blackledge M. Mapping protein conformational energy landscapes using NMR and molecular simulation. Chemphyschem. 2013; 14:3046–3058. [PubMed: 23703956]
53. Salmon L, Yang S, Al-Hashimi HM. Advances in the determination of nucleic acid conformational ensembles. Annu. Rev. Phys. Chem. 2014; 65:293–316. [PubMed: 24364917]
54. Meiler J, Prompers JJ, Peti W, Griesinger C, Bruschweiler R. Model-free approach to the dynamic interpretation of residual dipolar couplings in globular proteins. J. Am. Chem. Soc. 2001; 123:6098–6107. [PubMed: 11414844]
55. Tolman JR. A novel approach to the retrieval of structural and dynamic information from residual dipolar couplings using several oriented media in biomolecular NMR spectroscopy. J. Am. Chem. Soc. 2002; 124:12020–12030. [PubMed: 12358549]
56. Peti W, Meiler J, Bruschweiler R, Griesinger C. Model-free analysis of protein backbone motion from residual dipolar couplings. J. Am. Chem. Soc. 2002; 124:5822–5833. [PubMed: 12010057]

57. Ruan K, Briggman KB, Tolman JR. De novo determination of internuclear vector orientations from residual dipolar couplings measured in three independent alignment media. J. Biomol. NMR. 2008; 41:61–76. [PubMed: 18478335]
58. Yao L, Vogeli B, Torchia DA, Bax A. Simultaneous NMR study of protein structure and dynamics using conservative mutagenesis. J. Phys. Chem. B. 2008; 112:6045–6056. [PubMed: 18358021]
59. Wallach D. Effect of internal rotation on angular correlation functions. J. Chem. Phys. 1967; 47:5258–5268.
60. Lipari G, Szabo A. Nuclear magnetic rresonance relaxation in nucleic acid fragments - models for internal motion. Biochemistry. 1981; 20:6250–6256. [PubMed: 7306511]
61. Werbelow, LG.; Grant, DM. Intramolecular dipolar relaxation in multispin systems. In: Waugh, JA., editor. Advances in Magnetic Resonance. New York: Academic Press, Inc; 1977. p. 190-299.
62. Wittebort RJ, Szabo A. Theory of NMR relaxation in macromolecules - restricted diffusion and jump models for multiple internal rotations in amino-acid side-chains. J. Chem. Phys. 1978; 69:1722–1736.
63. Hubbard PS. Some properties of correlation functions of irreducible tensor operators. Physical Review. 1969; 180:319–326.
64. Woessner DE, Snowden BS, Meyer GH. Nuclear spin lattice relaxation in axially symmetric ellopsoids with internal motion. J. Chem. Phys. 1969; 50:719–721.
65. Lipari G, Szabo A. Model-free approach to the interpretation of nuclear magnetic resonance relaxation in macromolecules. 2. Analysis of experimental results. J. Am. Chem. Soc. 1982; 104:4559–4570.
66. Halle B. The physical basis of model-free analysis of NMR relaxation data from proteins and complex fluids. J. Chem. Phys. 2009; 131:224507–224528. [PubMed: 20001057]
67. Frederick KK, Sharp KA, Warischalk N, Wand AJ. Re-evaluation of the model-free analysis of fast internal motion in proteins using NMR relaxation. J. Phys. Chem. B. 2008; 112:12095–12103. [PubMed: 18759409]
68. Clore GM, Szabo A, Bax A, Kay LE, Driscoll PC, Gronenborn A. Deviation from the simple two-parameter model-free approach to the interpretation of nitrogeN-15 nuclear magnetic relaxation of proteins. J. Am. Chem. Soc. 1990; 112:4989–4991.
69. Wong V, Case DA, Szabo A. Influence of the coupling of interdomain and overall motions on NMR relaxation. Proc. Natl. Acad. Sci. USA. 2009; 106:11016–11021. [PubMed: 19541602]
70. Meirovitch E, Shapiro YE, Polimeno A, Freed JH. Structural dynamics of bio-macromolecules by NMR: The slowly relaxing local structure approach. Prog. Nucl. Magn. Reson. Spectrosc. 2010; 56:360–405. [PubMed: 20625480]
71. Emani PS, Olsen GL, Varani G, Drobny GP. Theory of nonrigid rotational motion applied to NMR relaxation in RNA (vol 115, pg 12055, 2011). J. Phys. Chem. A. 2012; 116:7253–7260. [PubMed: 22721263]
72. Gibby MG, Waugh JS, Pines A. Anisotropic nuclear spin relaxation of C-13 in solid benzene. Chem. Phys. Lett. 1972; 16:296–299.
73. Torchia DA, Szabo A. Spin-lattice relaxation in solids. J. Magn. Reson. 1982; 49:107–121.
74. Kurbanov R, Zinkevich T, Krushelnitsky A. The nuclear magnetic resonance relaxation data analysis in solids: General R-1/R-1 rho equations and the model-free approach. J. Chem. Phys. 2011; 135:184104. [PubMed: 22088049]
75. Jacobsen JP, Bildsoe HK, Schumburg K. Application of density matrix formalism in NMR spectroscopy. Ii. The one-spin-1 case in anisotropic phase. J. Magn. Res. 1976; 23:153–164.
76. Millet O, Muhandiram DR, Skrynnikov NR, Kay LE. Deuterium spin probes of sidechain dynamics in proteins. 1. Measurement of five relaxation rates per deuteron in C-13-labeled and fractionally H-2-enriched proteins in solution. J Am Chem Soc. 2002; 124:6439–6448. [PubMed: 12033875]
77. Skrynnikov NR, Millet O, Kay LE. Deuterium spin probes of side-chain dynamics in proteins. 2. Spectral density mapping and identification of nanosecond time-scale side-chain motions. J. Am. Chem. Soc. 2002; 124:6449–6460. [PubMed: 12033876]
78. Tugarinov V, Kay LE. Methyl groups as probes of structure and dynamics in NMR studies of high-molecular-weight proteins. ChemBioChem. 2005; 6:1567–1577. [PubMed: 16075427]

79. Atreya, HS. Adv exp med biol. New York: Springer; 2012. Isotope labeling in biomolecular NMR preface; p. 1-219.
80. Ottiger M, Bax A. Determination of relative N-H-N N-C ', C-alpha-C ', and C(alpha)-H-alpha effective bond lengths in a protein by NMR in a dilute liquid crystalline phase. J. Am. Chem. Soc. 1998; 120:12334–12341.
81. Ottiger M, Bax A. How tetrahedral are methyl groups in proteins? A liquid crystal NMR study. J. Am. Chem. Soc. 1999; 121:4690–4695.
82. Mittermaier A, Kay LE. Measurement of methyl H-2 quadrupolar couplings in oriented proteins. How uniform is the quadrupolar coupling constant? J. Am. Chem. Soc. 1999; 121:10608–10613.
83. Cornilescu G, Bax A. Measurement of proton, nitrogen, and carbonyl chemical shielding anisotropies in a protein dissolved in a dilute liquid crystalline phase. J. Am. Chem. Soc. 2000; 122:10143–10154.
84. Bryce DL, Grishaev A, Bax A. Measurement of ribose carbon chemical shift tensors for a-form RNA by liquid crystal NMR spectroscopy. J. Am. Chem. Soc. 2005; 127:7387–7396. [PubMed: 15898787]
85. Waddell KW, Chekmenev EY, Wittebort RJ. Single-crystal studies of peptide prolyl and glycyl N-15 shielding tensors. J. Am. Chem. Soc. 2005; 127:9030–9035. [PubMed: 15969580]
86. Ying JF, Grishaev A, Bryce DL, Bax A. Chemical shift tensors of protonated base carbons in helical RNA and DNA from NMR relaxation and liquid crystal measurements. J. Am. Chem. Soc. 2006; 128:11443–11454. [PubMed: 16939267]
87. Ying JF, Grishaev AE, Bax A. Carbon-13 chemical shift anisotropy in DNA bases from field dependence of solution NMR relaxation rates. Magn. Reson. Chem. 2006; 44:302–310. [PubMed: 16477676]
88. Yao LS, Vogeli B, Ying JF, Bax A. NMR determination of amide n-h equilibrium bond length from concerted dipolar coupling measurements. J. Am. Chem. Soc. 2008; 130:16518–16520. [PubMed: 19049453]
89. Wylie BJ, Schwieters CD, Oldfield E, Rienstra CM. Protein structure refinement using C-13 alpha chemical shift tensors. J. Am. Chem. Soc. 2009; 131:985–992. [PubMed: 19123862]
90. Grishaev A, Yao LS, Ying JF, Pardi A, Bax A. Chemical shift anisotropy of imino N-15 nuclei in watson-crick base pairs from magic angle spinning liquid crystal NMR and nuclear spin relaxation. J. Am. Chem. Soc. 2009; 131:9490–9491. [PubMed: 19537719]
91. Sheppard D, Li DW, Bruschweiler R, Tugarinov V. Deuterium spin probes of backbone order in proteins: H-2 NMR relaxation study of deuterated carbon alpha sites. J. Am. Chem. Soc. 2009; 131:15853–15865. [PubMed: 19821582]
92. Yao LS, Grishaev A, Cornilescu G, Bax A. Site-specific backbone amide N-15 chemical shift anisotropy tensors in a small protein from liquid crystal and cross-correlated relaxation measurements. J. Am. Chem. Soc. 2010; 132:4295–4309. [PubMed: 20199098]
93. Saito H, Ando I, Ramamoorthy A. Chemical shift tensor - the heart of NMR: Insights into biological aspects of proteins. Prog. Nucl. Magn. Reson. Spectrosc. 2010; 57:181–228. [PubMed: 20633363]
94. Tugarinov V. Indirect use of deuterium in solution NMR studies of protein structure and hydrogen bonding. Prog. Nucl. Magn. Reson. Spectrosc. 2014; 77:49–68. [PubMed: 24411830]
95. Yang DW, Venters RA, Mueller GA, Choy WY, Kay LE. Trosy-based hnco pulse sequences for the measurement of (HN)-H-1-N-15, N-15-(CO)-C-13, (HN)-H-1-(CO)-C-13, (CO)-C-13-C-13(alpha) and (HN)-H-1-C-13(alpha) dipolar couplings in N-15, C-13, H-2-labeled proteins. J. Biomol. NMR. 1999; 14:333–343.
96. Fitzkee NC, Bax A. Facile measurement of H-1-N-15 residual dipolar couplings in larger perdeuterated proteins. J. Biomol. NMR. 2010; 48:65–70. [PubMed: 20694505]
97. Ying JF, Wang JB, Grishaev A, Yu P, Wang YX, Bax A. Measurement of H-1-N-15 and H-1-C-13 residual dipolar couplings in nucleic acids from trosy intensities. J. Biomol. NMR. 2011; 51:89–103. [PubMed: 21947918]
98. Ying JF, Roche JL, Bax A. Homonuclear decoupling for enhancing resolution and sensitivity in noe and rdc measurements of peptides and proteins. J. Magn. Reson. 2014; 241:97–102. [PubMed: 24360766]

99. Liu YZ, Prestegard JH. A device for the measurement of residual chemical shift anisotropy and residual dipolar coupling in soluble and membrane-associated proteins. J. Biomol. NMR. 2010; 47:249–258. [PubMed: 20506033]
100. Palmer AG, Williams J, McDermott A. Nuclear magnetic resonance studies of biopolymer dynamics. J. Phys. Chem. 1996; 100:13293–13310.
101. Schanda P, Meier BH, Ernst M. Accurate measurement of one-bond h-x heteronuclear dipolar couplings in MAS solid-state NMR. J. Magn. Reson. 2011; 210:246–259. [PubMed: 21482161]
102. Hohwy M, Jaroniec CP, Reif B, Rienstra CM, Griffin RG. Local structure and relaxation in solid-state NMR: Accurate measurement of amide n-h bond lengths and h-n-h bond angles. J. Am. Chem. Soc. 2000; 122:3218–3219.
103. Asami S, Reif B. Proton-detected solid-state NMR spectroscopy at aliphatic sites: Application to crystalline systems. Acc. Chem. Res. 2013; 46:2089–2097. [PubMed: 23745638]
104. Shao L, Titman JJ. Chemical shift anisotropy amplification. Prog. Nucl. Magn. Reson. Spectrosc. 2007; 51:103–137.
105. Hung I, Gan ZH. An efficient amplification pulse sequence for measuring chemical shift anisotropy under fast magic-angle spinning. J. Magn. Reson. 2011; 213:196–199. [PubMed: 21962909]
106. Nirmala NR, Wagner G. Measurement of C-13 relaxation-times in proteins by two-dimensional heteronuclear h1-C-13 correlation spectroscopy. J. Am. Chem. Soc. 1988; 110:7557–7558.
107. Kay LE, Torchia DA, Bax A. Backbone dynamics of proteins as studied by 15N inverse detected heteronuclear NMR spectroscopy: Application to staphylococcal nuclease. Biochemistry. 1989; 28:8972–8979. [PubMed: 2690953]
108. Fischer MWF, Majumdar A, Zuiderweg ERP. Protein NMR relaxation: Theory, applications and outlook. Prog. Nucl. Magn. Reson. Spectrosc. 1998; 33:207–272.
109. Morin S. A practical guide to protein dynamics from N-15 spin relaxation in solution. Prog. Nucl. Magn. Reson. Spectrosc. 2011; 59:245–262. [PubMed: 21920220]
110. Chen K, Tjandra N. Water proton spin saturation affects measured protein backbone N-15 spin relaxation rates. J. Magn. Reson. 2011; 213:151–157. [PubMed: 22015249]
111. Lakomek NA, Ying J, Bax A. Measurement of N-15 relaxation rates in perdeuterated proteins by trosy-based methods. J. Biomol. NMR. 2012; 53:209–221. [PubMed: 22689066]
112. Yamazaki T, Muhandiram R, Kay LE. NMR experiments for the measurement of carbon relaxation properties in highly enriched, uniformly C-13,N-15-labeled proteins - application to C-13(alpha) carbons. J. Am. Chem. Soc. 1994; 116:8266–8278.
113. Zeng L, Fischer MWF, Zuiderweg ERP. Study of protein dynamics in solution by measurement of C-13(alpha)-(CO)-C-13 noe and (CO)-C-13 longitudinal relaxation. J. Biomol. NMR. 1996; 7:157–162. [PubMed: 22911008]
114. Chang SL, Tjandra N. Temperature dependence of protein backbone motion from carbonyl C-13 and amide N-15 NMR relaxation. J. Magn. Reson. 2005; 174:43–53. [PubMed: 15809171]
115. Lundstrom P, Teilum K, Carstensen T, Bezsonova I, Wiesner S, Hansen DF, Religa TL, Akke M, Kay LE. Fractional C-13 enrichment of isolated carbons using [1-C-13]- or [2-C-13]-glucose facilitates the accurate measurement of dynamics at backbone C-alpha and side-chain methyl positions in proteins. J. Biomol. NMR. 2007; 38:199–212. [PubMed: 17554498]
116. Wang TZ, Weaver DS, Cai S, Zuiderweg ERP. Quantifying Lipari-Szabo modelfree parameters from (CO)-C-13 NMR relaxation experiments. J. Biomol. NMR. 2006; 36:79–102. [PubMed: 17013680]
117. Hansen AL, Al-Hashimi HM. Dynamics of large elongated RNA by NMR carbon relaxation. J. Am. Chem. Soc. 2007; 129:16072–16082. [PubMed: 18047338]
118. Muhandiram DR, Yamazaki T, Sykes BD, Kay LE. Measurement of H-2 T-1 and T-1 rho relaxation-times in uniformly C-13 labeled and fractionally H-2-labeled proteins in solution. J. Am. Chem. Soc. 1995; 117:11536–11544.
119. Ishima R, Petkova AP, Louis JM, Torchia DA. Comparison of methyl rotation axis order parameters derived from model-free analyses of H-2 and C-13 longitudinal and transverse relaxation rates measured in the same protein sample. J. Am. Chem. Soc. 2001; 123:6164–6171. [PubMed: 11414851]

120. Sheppard D, Sprangers R, Tugarinov V. Experimental approaches for NMR studies of side-chain dynamics in high-molecular-weight proteins. Prog. Nucl. Magn. Reson. Spectrosc. 2010; 56:1–45. [PubMed: 20633347]
121. Cole HBR, Torchia DA. An NMR study of the backbone dynamics of staphylococcal nuclease in the crystalline state. Chem. Phys. 1991; 158:271–281.
122. Giraud N, Bockmann A, Lesage A, Penin F, Blackledge M, Emsley L. Site-specific backbone dynamics from a crystalline protein by solid-state NMR spectroscopy. J. Am. Chem. Soc. 2004; 126:11422–11423. [PubMed: 15366872]
123. Bertini I, Luchinat C, Parigi G, Ravera E, Reif B, Turano P. Solid-state NMR of proteins sedimented by ultracentrifugation. Proc. Natl. Acad. Sci. USA. 2011; 108:10396–10399. [PubMed: 21670262]
124. Huang W, Bardaro MF, Varani G, Drobny GP. Preparation of RNA samples with narrow line widths for solid state NMR investigations. J. Magn. Reson. 2012; 223:51–54. [PubMed: 22967888]
125. Tjandra N, Feller SE, Pastor RW, Bax A. Rotational diffusion anisotropy of human ubiquitin from 15N NMR relaxation. J. Amer. Chem. Soc. 1995; 117:12562–12566.
126. Massi F, Grey MJ, Palmer AG. Microsecond timescale backbone conformational dynamics in ubiquitin studied with NMR R-1 rho relaxation experiments. Protein Sci. 2005; 14:735–742. [PubMed: 15722448]
127. Lakomek NA, Carlomagno T, Becker S, Griesinger C, Meiler J. A thorough dynamic interpretation of residual dipolar couplings in ubiquitin. J. Biomol. NMR. 2006; 34:101–115. [PubMed: 16518697]
128. Lakomek NA, Walter KFA, Fares C, Lange OF, de Groot BL, Grubmuller H, Bruschweiler R, Munk A, Becker S, Meiler J, Griesinger C. Self-consistent residual dipolar coupling based model-free analysis for the robust determination of nanosecond to microsecond protein dynamics. J. Biomol. NMR. 2008; 41:139–155. [PubMed: 18523727]
129. Salmon L, Bouvignies G, Markwick P, Lakomek N, Showalter S, Li DW, Walter K, Griesinger C, Bruschweiler R, Blackledge M. Protein conformational flexibility from structure-free analysis of NMR dipolar couplings: Quantitative and absolute determination of backbone motion in ubiquitin. Angew. Chem. 2009; 48:4154–4157. [PubMed: 19415702]
130. Lorieau JL, McDermott AE. Conformational flexibility of a microcrystalline globular protein: Order parameters by solid-state NMR spectroscopy. J. Am. Chem. Soc. 2006; 128:11505–11512. [PubMed: 16939274]
131. Lange OF, Lakomek NA, Fares C, Schroder GF, Walter KFA, Becker S, Meiler J, Grubmuller H, Griesinger C, de Groot BL. Recognition dynamics up to microseconds revealed from an rdc-derived ubiquitin ensemble in solution. Science. 2008; 320:1471–1475. [PubMed: 18556554]
132. Clore GM, Schwieters CD. How much backbone motion in ubiquitin is required to account for dipolar coupling data measured in multiple alignment media as assessed by independent cross-validation? J. Am. Chem. Soc. 2004; 126:2923–2938. [PubMed: 14995210]
133. Markwick PRL, Bouvignies G, Salmon L, McCammon JA, Nilges M, Blackledge M. Toward a unified representation of protein structural dynamics in solution. J. Am. Chem. Soc. 2009; 131:16968–16975. [PubMed: 19919148]
134. Tolman JR. Structural biology protein dynamics from disorder. Nature. 2009; 459:1063–1064. [PubMed: 19553983]
135. Maltsev AS, Grishaev A, Roche J, Zasloff M, Bax A. Improved cross validation of a static ubiquitin structure derived from high precision residual dipolar couplings measured in a drug-based liquid crystalline phase. J. Am. Chem. Soc. 2014; 136:3752–3755. [PubMed: 24568736]
136. Rinaldelli M, Ravera E, Calderone V, Parigi G, Murshudov GN, Luchinat C. Simultaneous use of solution NMR and x-ray data in refmac5 for joint refinement/detection of structural differences. Acta Crystallographica Section D-Biological Crystallography. 2014; 70:958–967.
137. Babu YS, Bugg CE, Cook WJ. Structure of calmodulin refined at 2.2 A resolution. J. Mol. Biol. 1988; 204:191–204. [PubMed: 3145979]

138. Taylor DA, Sack JS, Maune JF, Beckingham K, Quiocho FA. Structure of a recombinant calmodulin from drosophila-melanogaster refined at 2.2-A resolution. J. Biol. Chem. 1991; 266:21375–21380. [PubMed: 1939171]

139. Chattopadhyaya R, Meador WE, Means AR, Quiocho FA. Calmodulin structure refined at 1.7 angstrom resolution. J. Mol. Biol. 1992; 228:1177–1192. [PubMed: 1474585]

140. Barbato G, Ikura M, Kay LE, Pastor R, Bax A. Backbone dynamics of calmodulin studied by 15N relaxation using inverse detected two-dimensional NMR spectroscopy: The central helix is flexible. Biochemistry. 1992; 31:5269–5278. [PubMed: 1606151]

141. Ikura M, Clore GM, Gronenborn AM, Zhu G, Klee CB, Bax A. Solution structure of a calmodulin-target peptide complex by multidimensional NMR. Science. 1992; 256:632–638. [PubMed: 1585175]

142. Meador WE, Means AR, Quiocho FA. Target enzyme recognition by calmodulin - 2.4-angstrom structure of a calmodulin-peptide complex. Science. 1992; 257:1251–1255. [PubMed: 1519061]

143. Baber JL, Szabo A, Tjandra N. Analysis of slow interdomain motion of macromolecules using NMR relaxation data. J. Am. Chem. Soc. 2001; 123:3953–3959. [PubMed: 11457145]

144. Kukic P, Camilloni C, Cavalli A, Vendruscolo M. Determination of the individual roles of the linker residues in the interdomain motions of calmodulin using NMR chemical shifts. J. Mol. Biol. 2014; 426:1826–1838. [PubMed: 24530797]

145. Bertini I, Del Bianco C, Gelis I, Katsaros N, Luchinat C, Parigi G, Peana M, Provenzani A, Zoroddu MA. Experimentally exploring the conformational space sampled by domain reorientation in calmodulin. Proc. Natl. Acad. Sci. USA. 2004; 101:6841–6846. [PubMed: 15100408]

146. Bertini I, Gupta YK, Luchinat C, Parigi G, Peana M, Sgheri L, Yuan J. Paramagnetism-based NMR restraints provide maximum allowed probabilities for the different conformations of partially independent protein domains. J. Am. Chem. Soc. 2007; 129:12786–12794. [PubMed: 17910448]

147. Bertini I, Giachetti A, Luchinat C, Parigi G, Petoukhov MV, Pierattelli R, Ravera E, Svergun DI. Conformational space of flexible biological macromolecules from average data. J. Am. Chem. Soc. 2010; 132:13553–13558. [PubMed: 20822180]

148. Anthis NJ, Doucleff M, Clore GM. Transient, sparsely populated compact states of apo and calcium-loaded calmodulin probed by paramagnetic relaxation enhancement: Interplay of conformational selection and induced fit. J. Am. Chem. Soc. 2011; 133:18966–18974. [PubMed: 21999431]

149. Bertini I, Luchinat C, Nagulapalli M, Parigi G, Ravera E. Paramagnetic relaxation enhancement for the characterization of the conformational heterogeneity in two-domain proteins. PCCP. 2012; 14:9149–9156. [PubMed: 22622816]

150. Rinnenthal J, Buck J, Ferner J, Wacker A, Furtig B, Schwalbe H. Mapping the landscape of RNA dynamics with NMR spectroscopy. Acc. Chem. Res. 2011; 44:1292–1301. [PubMed: 21894962]

151. Bardaro MF, Varani G. Examining the relationship between RNA function and motion using nuclear magnetic resonance. Wiley Interdisciplinary Reviews-RNA. 2012; 3:122–132. [PubMed: 22180312]

152. Emani PS, Olsen GL, Varani G, Drobny GP. Theory of nonrigid rotational motion applied to NMR relaxation in RNA. J. Phys. Chem. A. 2011; 115:12055–12069. [PubMed: 21870804]

153. Meirovitch E. The slowly relaxing local structure perspective of protein dynamics by NMR relaxation. Isr. J. Chem. 2014; 54:47–59.

154. Zhang Q, Sun XY, Watt ED, Al-Hashimi HM. Resolving the motional modes that code for RNA adaptation. Science. 2006; 311:653–656. [PubMed: 16456078]

155. Zhang Q, Al-Hashimi HM. Extending the NMR spatial resolution limit for RNA by motional couplings. Nat. Methods. 2008; 5:243–245. [PubMed: 18246076]

156. Chen Y, Campbell SL, Dokholyan NV. Deciphering protein dynamics from NMR data using explicit structure sampling and selection. Biophys. J. 2007; 93:2300–2306. [PubMed: 17557784]

157. Frank AT, Stelzer AC, Al-Hashimi HM, Andricioaei I. Constructing RNA dynamical ensembles by combining md and motionally decoupled NMR rdcs: New insights into RNA dynamics and adaptive ligand recognition. Nucleic Acids Res. 2009; 37:3670–3679. [PubMed: 19369218]

158. Dethoff EA, Hansen AL, Zhang Q, Al-Hashimi HM. Variable helix elongation as a tool to modulate RNA alignment and motional couplings. J. Magn. Reson. 2010; 202:117–121. [PubMed: 19854083]

159. Zweckstetter M, Bax A. Prediction of sterically induced alignment in a dilute liquid crystalline phase: Aid to protein structure determination by NMR. J. Am. Chem. Soc. 2000; 122:3791–3792.

160. Zweckstetter M. NMR: Prediction of molecular alignment from structure using the pales software. Nature Protocols. 2008; 3:679–690.

161. Sigel RKO, Sashital DG, Abramovitz DL, Palmer AG, Butcher SE, Pyle AM. Solution structure of domain 5 of a group ii intron ribozyme reveals a new RNA motif. Nat. Struct. Mol. Biol. 2004; 11:187–192. [PubMed: 14745440]

162. Zweckstetter M, Hummer G, Bax A. Prediction of charge-induced molecular alignment of biomolecules dissolved in dilute liquid-crystalline phases. Biophys. J. 2004; 86:3444–3460. [PubMed: 15189846]

163. Eichhorn CD, Feng J, Suddala KC, Walter NG, Brooks CL, Al-Hashimi HM. Unraveling the structural complexity in a single-stranded RNA tail: Implications for efficient ligand binding in the prequeuosine riboswitch. Nucleic Acids Res. 2012; 40:1345–1355. [PubMed: 22009676]

164. Salmon L, Bascom G, Andricioaei I, Al-Hashimi HM. A general method for constructing atomic-resolution RNA ensembles using NMR residual dipolar couplings: The basis for interhelical motions revealed. J. Am. Chem. Soc. 2013; 135:5457–5466. [PubMed: 23473378]

165. Olsen GL, Bardaro MF, Echodu DC, Drobny GP, Varani G. Hydration dependent dynamics in RNA. J. Biomol. NMR. 2009; 45:133–142. [PubMed: 19669102]

166. Olsen GL, Echodu DC, Shajani Z, Bardaro MF, Varani G, Drobny GP. Solid-state deuterium NMR studies reveal mu s-ns motions in the HIV-1 transactivation response RNA recognition site. J. Am. Chem. Soc. 2008; 130:2896–2897. [PubMed: 18275190]

167. Olsen GL, Bardaro MF, Echodu DC, Drobny GP, Varani G. Intermediate rate atomic trajectories of RNA by solid-state NMR spectroscopy. J. Am. Chem. Soc. 2010; 132:303–308. [PubMed: 19994901]

168. Emani PS, Olsen GL, Echodu DC, Varani G, Drobny GP. Slow exchange model of nonrigid rotational motion in RNA for combined solid-state and solution NMR studies. J. Phys. Chem. B. 2010; 114:15991–16002. [PubMed: 21067190]

169. Emani PS, Bardaro MF, Huang W, Aragon S, Varani G, Drobny GP. Elucidating molecular motion through structural and dynamic filters of energy-minimized conformer ensembles. J. Phys. Chem. B. 2014; 118:1726–1742. [PubMed: 24479561]

170. Yuwen T, Post CB, Skrynnikov NR. Domain cooperativity in multidomain proteins: What can we learn from molecular alignment in anisotropic media? J. Biomol. NMR. 2011; 51:131–150. [PubMed: 21947922]

171. Keizers PM, Ubbink M. Paramagnetic tagging for protein structure and dynamics analysis. Prog. Nucl. Magn. Reson. Spectrosc. 2011; 58:88–96. [PubMed: 21241885]

172. Koehler J, Meiler J. Expanding the utility of NMR restraints with paramagnetic compounds: Background and practical aspects. Prog. Nucl. Magn. Reson. Spectrosc. 2011; 59:360–389. [PubMed: 22027343]

173. Al-Hashimi HM. NMR studies of nucleic acid dynamics. J. Magn. Reson. 2013; 237:191–204. [PubMed: 24149218]

Glossary

AMD	Accelerated molecular dynamics
CS	Chemical shift
CaM	Calmodulin
D	Dipolar

EMF	Extended model free
GAF	Gaussian axial fluctuation
GE	General exchange
L-frame	Laboratory frame
MAS	Magic angle spinning
MD	Molecular dynamics
MF	Model free
M-frame	Intermediate frame
MFRDC	Model free residual dipolar coupling
MO	Maximum occurrence
PAS	Principal axis system
PCS	Pseudocontact shift
PDB	Protein data bank
P-frame	Principal axis frame
PRE	Paramagnetic relaxation enhancement
Q	Quadrupole
RCSA	Residual chemical shift anisotropy
RDC	Residual dipole coupling
REDOR	Rotational echo double resonance
RQC	Residual quadrupole coupling
SCRM	Self-consistent model free
SFGAF	Structure free Gaussian axial fluctuation
SVD	Singular value decomposition
TAR	HIV-1 transactivation response element RNA

Manuscript Highlights

Averaging of spin interactions by molecular motion

Molecular motion and spin relaxation

Molecular dynamics of ubiquitin

Domain dynamics of calmodulin

Dynamics of the HIV-1 trans-activation response element RNA

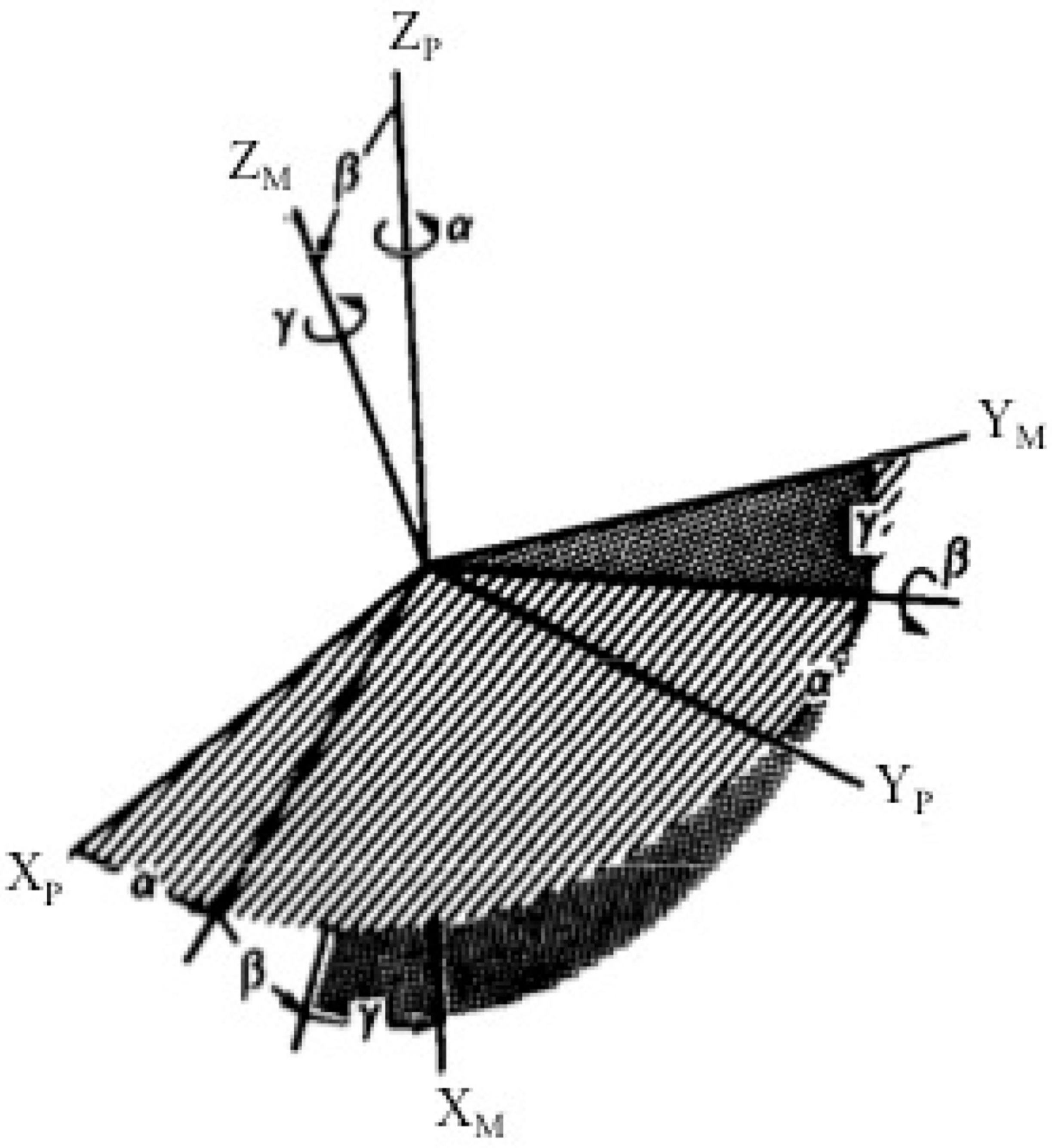

Fig. 1.

Illustration of the rotation through the Euler angles (α_{PM}, β_{PM}, γ_{PM}) that brings the principal axis system (X_P, Y_P, Z_P) into coincidence with the M-frame coordinate system (X_M, Y_M, Z_M). In the case of the dipolar tensor, the symmetry axis, $\boldsymbol{\mu}$, is along Z_P. For clarity the subscripts on the Euler angles are omitted in the drawing. A second rotation through Euler angles (α_{ML}, β_{ML}, γ_{ML}) brings the M-frame coordinate system into coincidence with the L-frame (X_L, Y_L, Z_L), where Z_L is along $\boldsymbol{\mu}_B$. One obtains the elements of interaction tensor in the L-frame, R^{λ}_{2m}, from the measured values of the interaction tensor elements in the P-frame, $\rho^{\lambda}{}_{2m}$, (Table 1) using Wigner rotation matrix elements according to Eq. (3). The definition of the Euler angles is that given in references [23, 26].

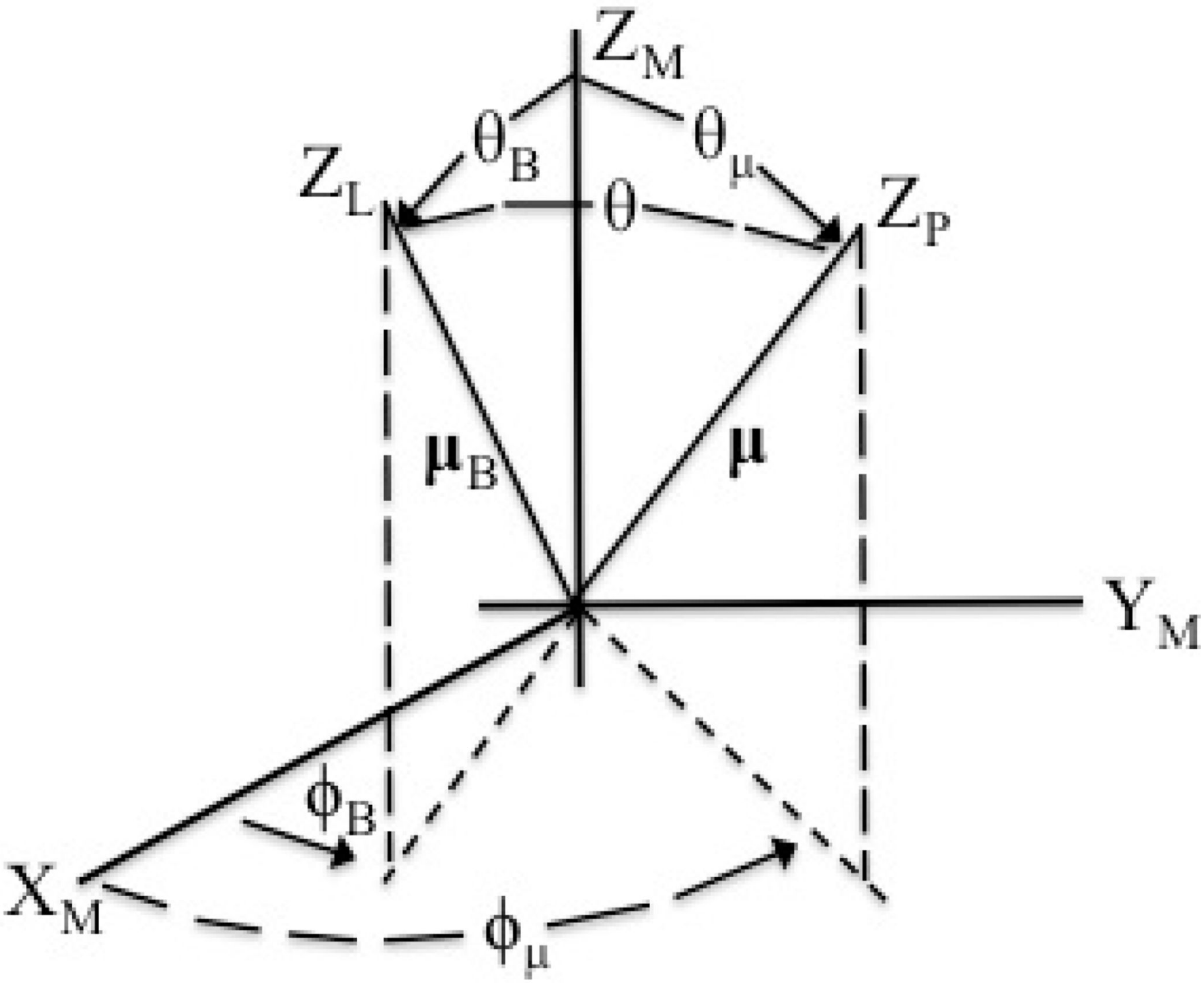

Fig. 2.

Illustration of the spherical polar angles (θ_B, φ_B) and (θ_μ, φ_μ) that specify the orientations of the external magnetic field, $\boldsymbol{\mu}_B$, and the N-H bond axis, $\boldsymbol{\mu}$, in the M-frame. The relationship between these angles and θ, the angle subtended by unit vectors $\boldsymbol{\mu}_B$ and $\boldsymbol{\mu}$, is also shown.

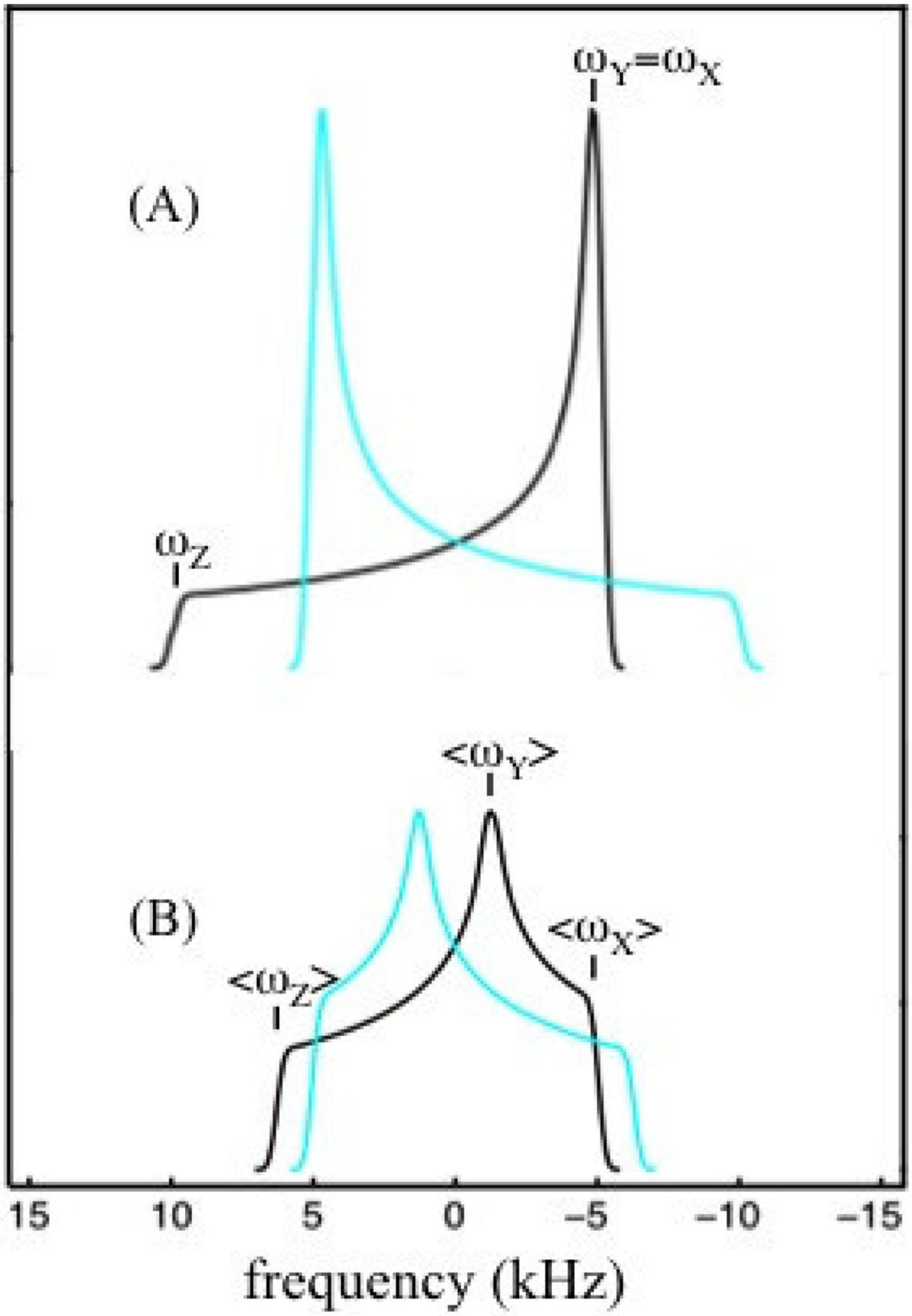

Fig. 3.

(A) Solid-state NMR spectrum of a spin-1/2 nucleus such as ^{15}N that has a dipolar interaction with a single ^{1}H spin (with $-\omega_D/\pi = 20$ kHz; for simplicity, the chemical shift anisotropy is not considered.) Two distributions of dipolar couplings one corresponding to the α spin-states of the proton and the other to the β are superimposed giving rise to the "Pake doublet" lineshape. The frequency distribution results from the angular dependence of the dipolar interaction, Eq. (3). The positions of principal frequencies (ω_X, ω_Y, ω_Z) are indicated by short vertical lines, with conventions $|\omega_Z| \geq |\omega_X| \geq |\omega_Y|$ and $\Sigma\omega_i = 0$, i = X, Y,

Z. The frequency having the largest magnitude ω_Z occurs when the NH bond is parallel to B_o, while the other principal frequencies $\omega_X = \omega_Y = -\omega_Z/2$ occur when the NH bond is perpendicular to B_o. In the absence of motions, the maximum dipolar splitting, $D_m = -\omega_D/\pi$ is here assumed to be 20 kHz. (B) Reorientation of the NH bond on a timescale $t << 1/\omega_D$ averages the frequency distribution, resulting in a narrowing of the static powder patterns. The averaged powder patterns in (B) result when the N-H bond jumps between two equally-populated orientations which differ by 60°. The axially asymmetric motion in this example results in an averaged dipolar tensor that is asymmetric, yielding asymmetric powder patterns in which the principal frequencies are not degenerate. S^2 can be calculated using Eq. (17) and the principal frequencies obtained from the lineshapes in (A) and (B). In the same manner, S^2 can be derived for axially symmetric chemical shifts of spin-1/2 or from quadrupolar interactions of ^2H that are dynamically averaged. Although contemporary high-resolution solid-state experiments of biomolecules are recorded with MAS, recoupling approaches can recover the information contained in anisotropic line shapes, while providing high resolution spectra as discussed in the text.

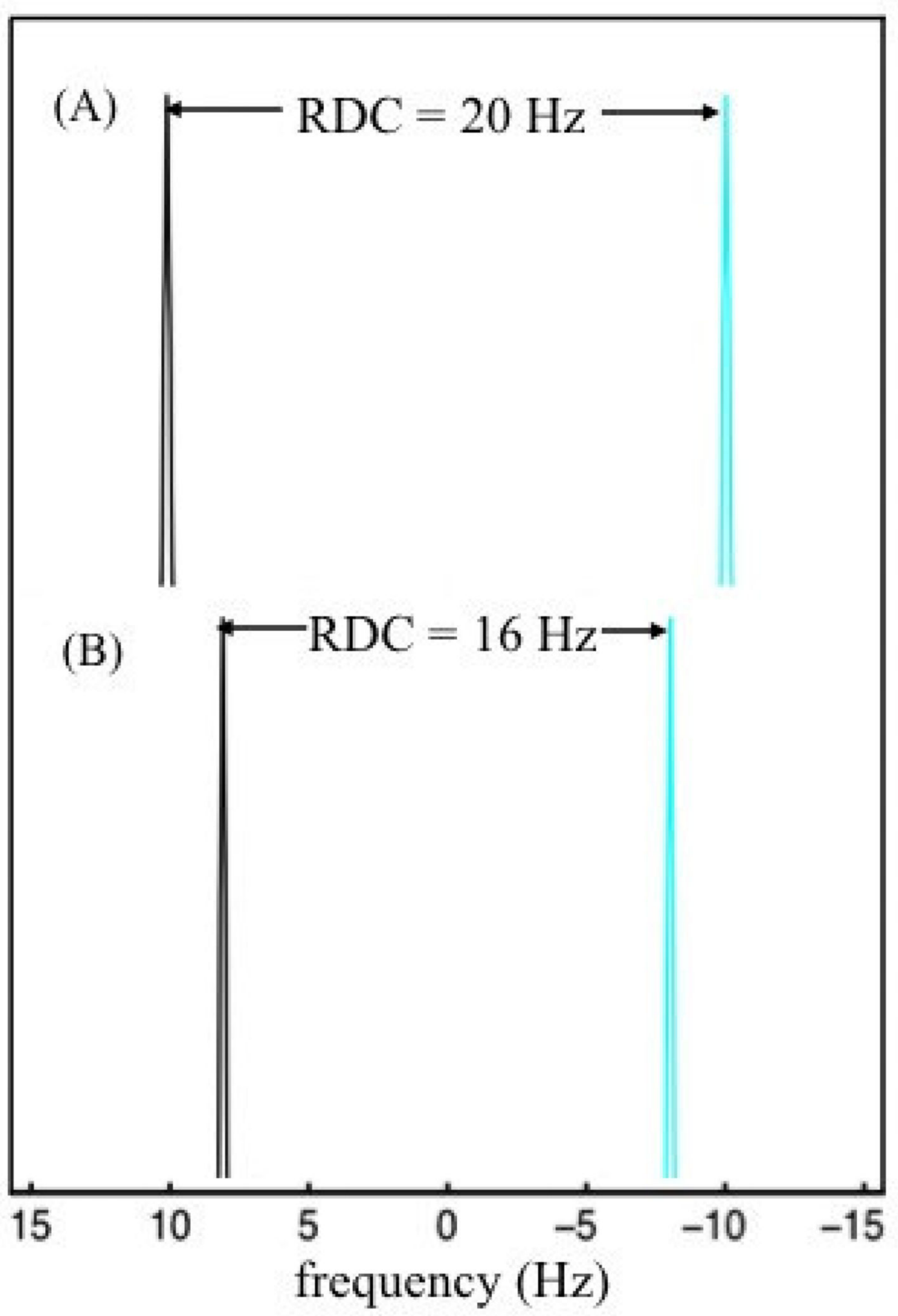

Fig. 4.

In an isotropic liquid, the quantities $<C_{2q}{}^*(\Omega_B)>$ on the right side of Eq. (10) vanish, along with all RDCs, as a consequence of overall molecular tumbling on a timescale, $\tau_c < 10^{-7}$ s. However this is not the case for an aligned sample, because $\boldsymbol{\mu}_B$ assumes a non-uniform distribution in the M-frame, and RDCs are then given by Eq. (20). (A) Illustrates the maximum dipolar splitting for the case of an N-H dipolar interaction with, D_{max} = 20 kHz, A_a = .001 which occurs when $\theta_{\mu j}$ = 0°. Other NH orientations exhibit smaller RDCs. (B) illustrates the reduction, in the RDC shown in (A) that results from diffusion (on a timescale

$< 10^{-3}$ s) of the NH bond in a cone with semi angle 30°, centered at $\theta_{\mu j} = 0°$, in which case $S = 0.8$.

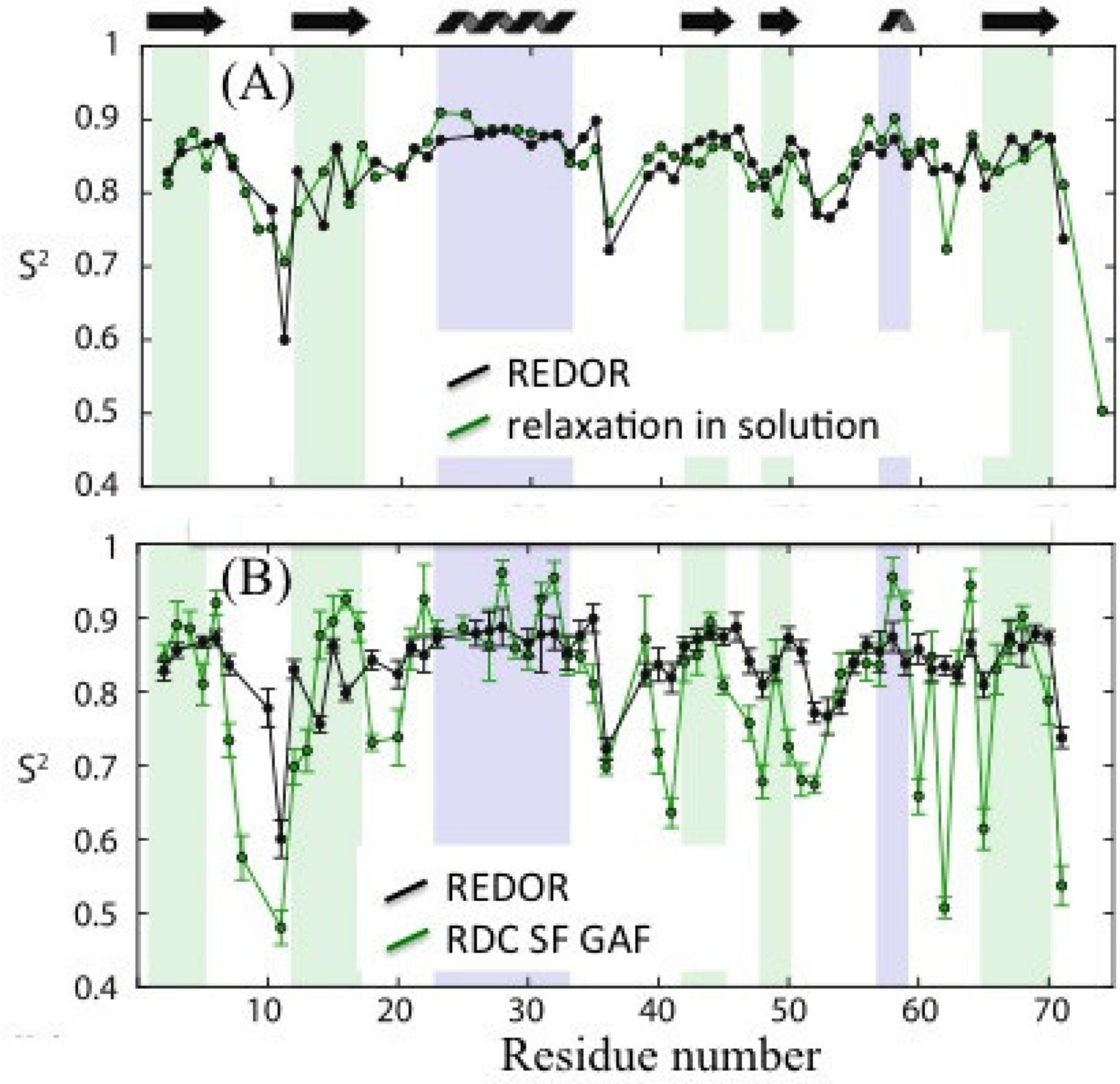

Fig. 5.

Plots comparing amide N-H MF order parameters obtained from REDOR measurements of crystalline ubiquitin with those obtained in solution; (A) S^2 from REDOR [14] (black) and from ^{15}N relaxation measurements in solution (green), and (B) S^2 from REDOR [14] (black) and from a structure-free GAF analysis of RDC measurements in solution [129] (green). Figure adapted from Haller and Schanda [14].

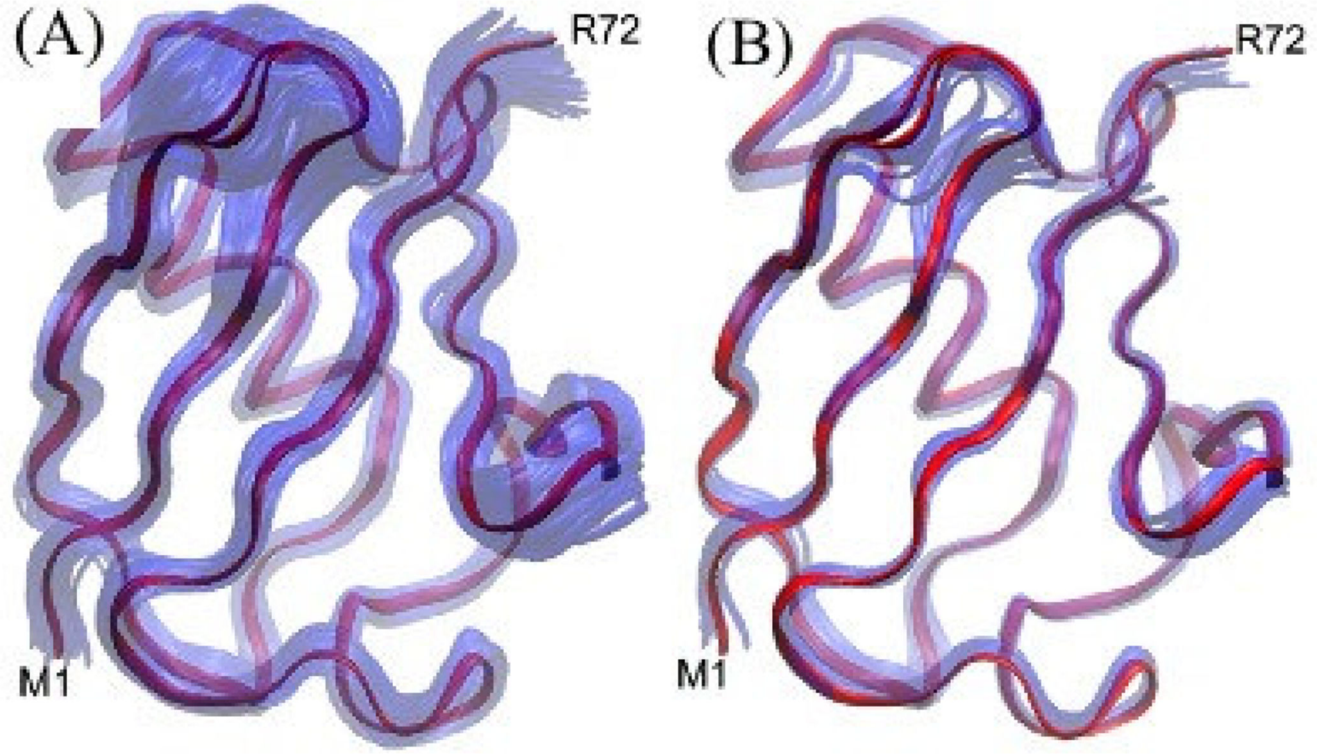

Fig. 6.

Overlaid backbone representations of the recently derived NMR structure 2MJB (red) with (A) the RDC ensemble representation 2KOX (in transparent blue), and (B) with the 15 highest-resolution X-ray structures of ubiquitin (also in transparent blue). The structures were superimposed by best-fitting the residues with most-ordered backbone coordinates in the X-ray ensemble as described by Maltsev *et al.* [135], from whom the Figure is adapted.

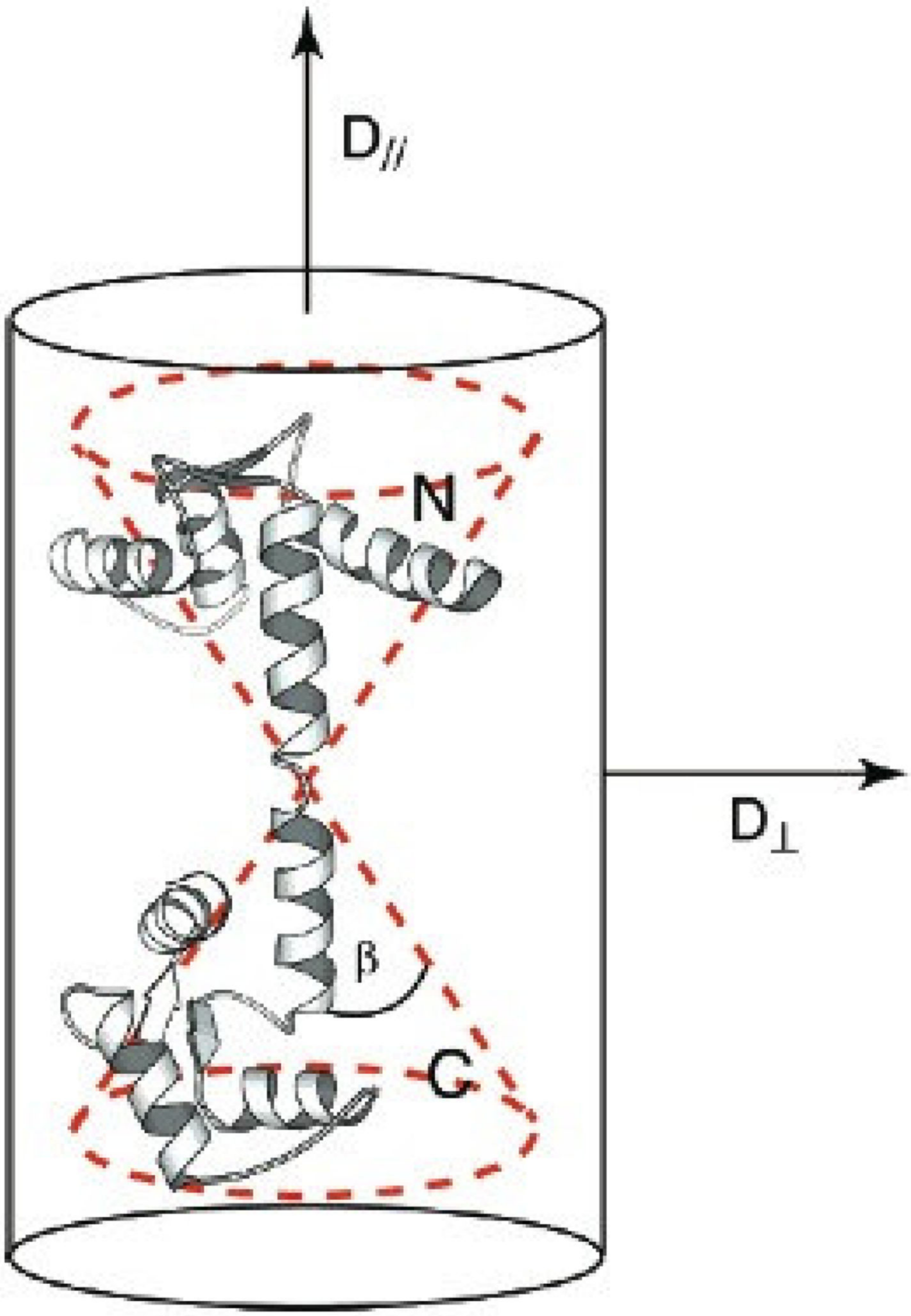

Fig. 7.

A ribbon diagram [143] of the fully extended $4Ca^{2+}$CaM structure generated from the coordinates of PDB accession number 3CLN. $D_\parallel$ and $D_\perp$ represent the components of the axially symmetric overall diffusion tensor of the extended structure. The angle β characterizes the amplitude of internal domain motion derived from EMF order parameters interpreted using the diffusion in a cone model. Figure adapted from Baber *et al*. [143]

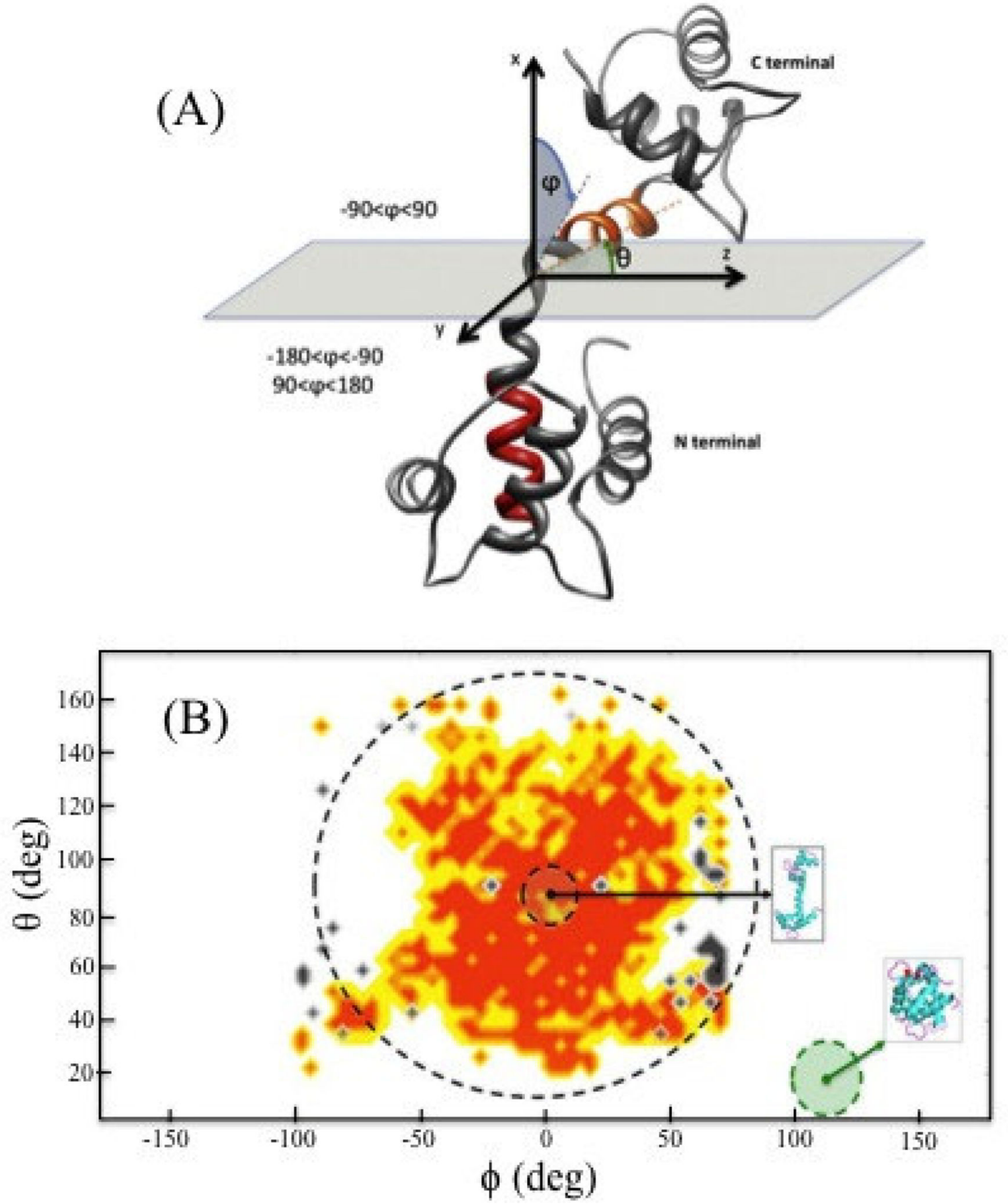

Fig. 8.

(A) Illustration of the spherical polar coordinates used to represent the orientations of α-helix V (orange) relative to α-helix IV (red) in the respective C- and N-terminal domains of $4Ca^{2+}CaM$ [144] (B) Comparison of the distributions of (θ, φ) angles sampled by the chemical shift (yellow-red scale), PRE (grey scale), and peptide-bound X-ray (green circle) ensembles of $4Ca^{2+}CaM$ conformations. Figure adapted from Kukic *et al*. [144].

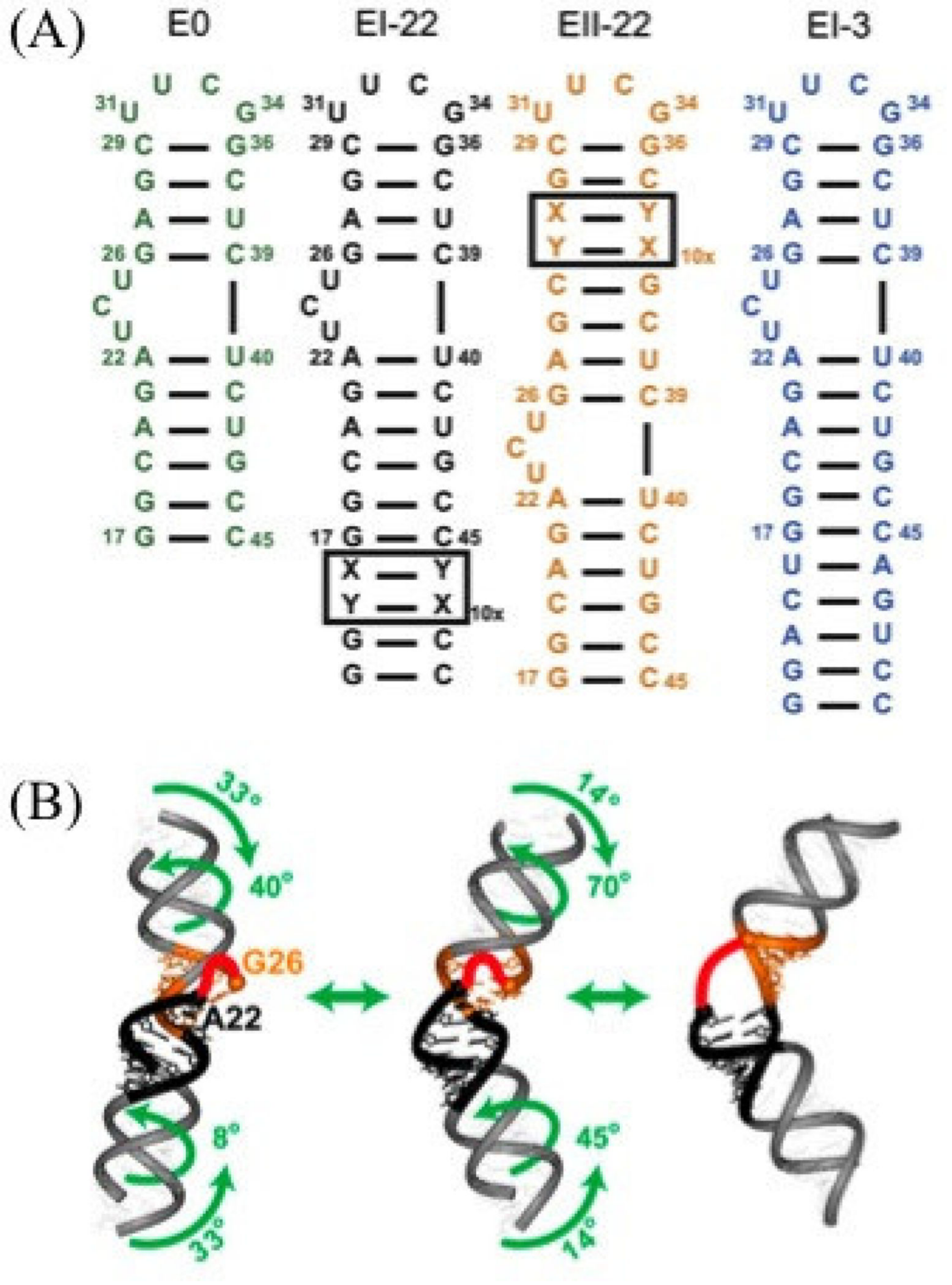

Fig. 9.

(A) Secondary structure of TAR, E0, and three elongated TAR constructs EI-22, EII-22 and EI-3 used to measure independent sets of RDCs [173]. (B) Three-state TAR ensemble [173] used to fit RDCs of elongated TAR constructs. Figure adapted from Al-Hashimi *et al*. [173].

Table 1

Factors[a] C^{λ}, spin-dependent operators[b] T_{20}^{λ}, and interaction-tensor elements ρ_{2m}^{λ}, in the tensor principal axis system.

Interaction	λ	C^{λ}	T_{20}^{λ}	ρ_{20}^{λ}	$\rho_{2\pm1}^{\lambda}$	$\rho_{2\pm2}^{\lambda}$
Dipole-dipole	D	$-(\mu_0/2\pi)\hbar\,\gamma_I\gamma_S$	$[3\hat{I}_Z\hat{S}_Z - \hat{I}\bullet\hat{S}]/6^{1/2}$	$(3/2)^{1/2}r_{IS}^{-3}$	0	0
Chemical Shift[c]	CS	γ_S	$(2/3)^{1/2}\hat{S}_Z B_0$	$(2/3)^{1/2}\Delta\sigma$	0	$-\Delta\sigma\eta_{CS}/3$
Quadrupole	Q	$eQ/2\hbar$	$\left[3\hat{S}_Z^2 - S(S+1)\right]/6^{1/2}$	$(3/2)^{1/2}\,eq$	0	$-eq\eta_Q/2$

[a] μ_0 is the permeability of free space and other symbols are defined by Spiess[23].

[b] The secular part of T_{20}^{D} equals $(2/3)^{1/2}\hat{I}_Z\hat{S}_Z$. The operators $T_{2\pm1}^{\lambda}, T_{2\pm2}^{\lambda}$ are given by Spiess[23]. They are not listed because they do not explicitly appear in subsequent equations herein.

[c] H_{CS} contains contributions from first rank tensors. However, they are insignificant for the nuclei of interest herein.

Table 2

Experimental validation statistics for different structural representations of ubiquitin.[a]

Structure	**2MJB**[c]	**2KOX**[d]	**<X-ray>**[e]
RCSA[b] (ppb)	6.5/15.7/8.9[b]	9.2/17.5/11.1[b]	6.2/13.9/8.1[b]
Q_{CC}(%)	9.3/22.2/11.7	10.5/21.1/12.4	9.9/14.3/10.4
$^3J_{HNH}$[f] (Hz)	0.43/0.77/0.50	0.58/0.89/0.65	0.50/0.83/0.57

[a] For residues Q2-V70. Results derived from Table 1 of Maltsev et al. [135].

[b] The first number corresponds to residues with rmsd ≤ 0.4 Å for backbone coordinates (N, C_α, C') in the X-ray ensemble; the second number to residues with rmsd > 0.4 Å (7–11, 32–35, 46, 47, 52 and 70); the third number to all residues.

[c] Maltsev et al. [135].

[d] Fenwick et al. [50].

[e] Ensemble of 15 chains from high resolution (≤1.8Å) X-ray structures [135].